Research in Astronomy and Astrophysics, 25:035010 (21pp), 2025 March
https://doi.org/10.1088/1674-4527/adae46
CSTR: 32081.14.RAA.adae46
© 2025. National Astronomical Observatories, CAS and IOP Publishing Ltd. All rights, including for text and data mining, AI training, and similar technologies, are reserved. Printed in China.

Tests of Solar X-Ray Image Reconstruction: Study of X-Ray Imaging Algorithms and Reconstruction Parameters

Wenhui Yu[1,2], Yang Su[1,2], Zhentong Li[1], Wei Chen[1,2], and Weiqun Gan[1,3]
[1] Key Laboratory of Dark Matter and Space Astronomy, Purple Mountain Observatory, Chinese Academy of Sciences, Nanjing 210023, China; yang.su@pmo.ac.cn
[2] School of Astronomy and Space Science, University of Science and Technology of China, Hefei 230026, China
[3] University of Chinese Academy of Sciences (UCASNJ), Nanjing 211135, China
Received 2024 November 22; revised 2025 January 10; accepted 2025 January 14; published 2025 March 10

Abstract

Imaging observations of solar X-ray bursts can reveal details of the energy release process and particle acceleration in flares. Most hard X-ray imagers make use of the modulation-based Fourier transform imaging method, an indirect imaging technique that requires algorithms to reconstruct and optimize images. During the last decade, a variety of algorithms have been developed and improved. However, it is difficult to quantitatively evaluate the image quality of different solutions without a true, reference image of observation. How to choose the values of imaging parameters for these algorithms to get the best performance is also an open question. In this study, we present a detailed test of the characteristics of these algorithms, imaging dynamic range and a crucial parameter for the CLEAN method, clean beam width factor (CBWF). We first used SDO/AIA EUV images to compute DEM maps and calculate thermal X-ray maps. Then these realistic sources and several types of simulated sources are used as the ground truth in the imaging simulations for both RHESSI and ASO-S/HXI. The different solutions are evaluated quantitatively by a number of means. The overall results suggest that EM, PIXON, and CLEAN are exceptional methods for sidelobe elimination, producing images with clear source details. Although MEM_GE, MEM_NJIT, VIS_WV and VIS_CS possess fast imaging processes and generate good images, they too possess associated imperfections unique to each method. The two forward fit algorithms, VF and FF, perform differently, and VF appears to be more robust and useful. We also demonstrated the imaging capability of HXI and available HXI algorithms. Furthermore, the effect of CBWF on image quality was investigated, and the optimal settings for both RHESSI and HXI were proposed.

Key words: techniques: image processing – Sun: flares – Sun: X-rays, gamma rays

1. Introduction

X-ray emissions in solar flares are mostly from thermal and non-thermal bremsstrahlung (e.g., Brown et al. 1998; Holman et al. 2011). X-ray observations of solar flares, X-ray imaging in particular, are thought to be a powerful tool to investigate mechanisms of magnetic reconnection, particle acceleration, plasma heating and energy transfer process.

Most solar X-ray imagers employ an indirect, Fourier-transform imaging technique. They modulate incident X-rays with a group of subcollimators, each one consisting of a pair of grids installed in the front and rear panels. Modulation profiles can be obtained in temporal space via rotating subcollimators with different pitches or in spatial orientation via arranging a combination of subcollimators that have different positioning angles, pitches, and phases. The Reuven Ramaty High Energy Solar Spectroscopic Imager (RHESSI, 2002–2018, Lin et al. 2002) is one of the successful applications of time modulation. It spins every 4 s to get full coverage of positioning angles of grids. Spatial modulation is often used in comprehensive missions where stabilized platforms are required for direct, optical imaging in other wavelengths, such as, Yohkoh/Hard X-ray Telescope (HXT. Kosugi et al. 1991), the Spectrometer/Telescope for Imaging X-rays (STIX, Krucker et al. 2020) aboard the Solar Orbiter and Hard X-ray Imager (HXI, Su et al. 2019, 2024; Zhang et al. 2019) aboard the ASO-S (Gan et al. 2019, 2023) mission.

In recent years, NuSTAR (Harrison et al. 2013) (designed for astrophysical observations) and FOXSI (Krucker et al. 2014) (rocket experiment) utilized direct-focusing optics to attain much higher sensitivity in hard X-ray imaging. However, the application of this method in regular solar observations is still under development.

For indirect HXR imaging, algorithms are also essential. X-ray photons passing through a modulation imager are recorded by the detectors behind bi-grid subcollimators that have different pitches, phases, and positioning angles. The transmittance of photons or measured counts of different subcollimators (modulation profiles) contains information about different aspects of the sources (location, intensity, size, etc.). X-ray images are reconstructed from these data by imaging algorithms. Thus this imaging process is an inverse problem of deducing the source geometry from a modulation profile with limited data.

In general, there are two types of reconstruction methods: one is based on visibilities, and the other is based on patterns. Visibilities, which are the Fourier components of a spatial flux distribution converted from modulation profiles and calibrated (Hurford et al. 2002; Hannah et al. 2008), represent the Fourier components of X-ray sources in the two-dimensional Fourier space known as the (u, v) plane. Patterns are the responses of subcollimators to point sources at each location (x, y) in their field of view (FOV). Algorithms based on patterns compute the source image directly from modulated counts.

More than ten image reconstruction algorithms have been developed for RHESSI software. They are often used for different scientific applications. A test of these methods and a brief summary can be found in Dennis & Tolbert (2019), Piana et al. (2022) and at https://hesperia.gsfc.nasa.gov/rhessi3/software/imaging-software/image-algorithm-summary/index.html. However, it is usually difficult to draw solid conclusions from this type of test for three reasons, (a) these methods may be used for different scientific purposes and applications; (b) there are no ground truth images for evaluation or comparison (except in imaging simulations); (c) it is difficult to quantitatively evaluate the quality of reconstructed images.

In this paper, we tested ten algorithms that have been developed for the analysis of RHESSI data. In order to get the ground truth images, we used Atmospheric Imaging Assembly (AIA, Lemen et al. 2012) data to obtain (thermal) X-ray images through the differential emission measure (DEM) method (Cheung et al. 2015; Su et al. 2018; Li et al. 2022, here we call it DEM-X method). Studies have shown that accurate DEM results can be used to produce soft X-ray images (Su et al. 2018) and to estimate the detailed density distribution along a flaring loop for quantitative study of electron transport (Li et al. 2022). On the other hand, we compute reduced χ^2, C-statistic (Cstat), and QuIX index (a new quantitative method named Quality Index of X-ray images which also takes into account the effect of sidelobes, Li et al. 2024) of the results to estimate the imaging quality. Using RHESSI data and software, we tested four cases: DEM-based simulation test, double sources, dynamic range test, and CLEAN beam width factor (CBWF) test. In addition, we also tested the algorithms available for HXI with observational data, DEM-based simulation and dynamic range simulation. Using QuIX index, we further studied the effect of CBWF on imaging results and found the best default setting for both RHESSI and HXI. This work is important for improving our understanding of different imaging algorithms and also useful for the development of the algorithms for HXI.

2. Imaging Algorithms

Here we present a short introduction on the imaging algorithms tested in this work. For a more detailed description, we refer the readers to Piana et al. (2022).

The most straightforward image reconstruction method is Backprojection, i.e., BP (Mertz et al. 1986), where modulation profiles or visibilities are added linearly to get the so-called dirty map. There are always sidelobes in the dirty map because of the instrumental effect from indirect imaging. Thus, more imaging algorithms have been developed to improve image quality.

CLEAN (Högbom 1974) is a widely used iterative algorithm in radio and hard X-ray imaging based on the assumption that an image can be well represented by a superposition of multiple point sources (Hurford et al. 2002). It starts from the dirty map as the initial image. The iterative process successively picks up the brightest points in the image as CLEAN components and subtracts a fraction of the point-spread function (PSF) centered at the selected location from the dirty map. The process repeats over the remaining image (residual image), trying to remove as many sidelobes as possible. The final CLEAN image comes from the CLEAN components convolved with a CLEAN beam with a certain beam size, plus the final remaining residual image. Different ways of adding back residual images were proposed in Dennis & Tolbert (2019).

Expectation maximization (EM, Benvenuto et al. 2013) is a statistical iterative method that searches for the flux distribution that maximizes the probability of the observation under the constraint that the pixel content must be positive. The STIX version of EM is available now (Massa et al. 2019).

Pixon (Metcalf et al. 1996) was originally an algorithm developed for Yohkoh/HXT, from which RHESSI's version was derived. This approach uses fewer pixons to minimize degrees of freedom and maximize the use of limited data, but it takes longer time to reconstruct images.

The forward-fitting (FF) method (Aschwanden et al. 2002, 2004) is a parameterization modeling method that posits the existence of one or more sources with specific shapes within an image. Source structures are usually quantified by circular Gaussians, elliptical Gaussians, or curved elliptical Gaussians (i.e., loop shapes). The image process determines the best-fit parameters through comparison of the predicted modulation profiles (from assumed sources) with those observed. The visibility forward fit (VF, Hurford et al. 2005; Hannah et al. 2008) algorithm also necessitates a prior hypothesis regarding the number and shape of sources. In addition, it allows for greater flexibility in setting the initial values of the source flux, centroid location, width, and angle or fixing them as constant parameters before commencing the fitting process, which helps to effectively constrain the imaging process. Flux, area, and other source parameters, along with their corresponding uncertainties, can be easily derived through the VF method (Dennis & Pernak 2009).

Maximum Entropy Method (MEM) algorithms maximize the information entropy while minimizing a measure of the goodness of fit (usually reduced χ^2) and maintaining the correct value of the flux (Schmahl et al. 2007). Visibility-based

MEM_NJIT was developed at the New Jersey Institute of Technology (NJIT). Sometimes it produces images with multiple unrealistically small sources and shows a super-resolution phenomenon (Dennis & Pernak 2009). MEM_GE (Massa et al. 2020) optimizes this problem while maintaining the advantages of MEM_NJIT.

UV_Smooth (Massone et al. 2009) involves spline interpolation at spatial frequencies. It proceeds by smoothing the observed visibilities in the spatial frequency plane, to broaden the available set of Fourier components used in Fourier inversion that leads to the final image.

VIS_CS (Felix et al. 2017) is a compressed sensing image reconstruction method. It assumes that solar flares can be represented by a linear combination of a few scaled and rotated two-dimensional Gaussian distributions. VIS_CS strives to generate realistic images that align with the measurements, thereby frequently obtaining favorable Cstat outcomes.

VIS_WV (Duval-Poo et al. 2018) is another compressed sensing method utilizing finite isotropic wavelets. It considers X-ray sources to be either isotropic or having a slowly varying shape, without relying on prior knowledge of specific shapes compared to VIS_CS.

3. Data Processing and Preparation

3.1. Evaluations of Reconstructed Images

In this work, we considered three metrics to evaluate the quality of reconstructed images: Cstat (Cash 1979), reduced χ^2 and QuIX (Li et al. 2024).

In general, smaller Cstat and χ^2 mean better image quality. However, they cannot reflect all aspects of images in some cases. QuIX (Li et al. 2024) is a new method developed to quantitatively evaluate X-ray imaging quality, which is a composite parameter that contains three indices: root mean square error (RMSE), structural similarity index measure (SSIM) and percentage proximity degree (PPD). An important feature of X-ray imaging is the presence of sidelobes and artifacts. The PPD is a parameter specifically designed to measure the extent of sidelobes, taking into account the number of pixels above a threshold of the maximum value of the map. SSIM and RMSE are used to measure the structure of the source, including the shape, size, position, and orientation of the source. Li et al. (2024) evaluated multiple existing image quality assessment methods for different grid settings and source structures, and selected the most representative ones, SSIM and RMSE. Then the Technique for Order Preference by Similarity to Ideal Solution (TOPSIS, Hwang & Yoon 1981) was used to order the samples based on a decision matrix formed by the three indices and then to weight the three indices to formulate QuIX.

QuIX value can only be obtained by simultaneously inputting reconstructed images and model image (the ground truth). The range of QuIX values is from 0 to 1, where higher values indicate better imaging quality. QuIX of 1 means that the two images are identical.

To avoid possible contributions of non-thermal bremsstrahlung and saturated extreme ultraviolet (EUV) images, we selected two B-class flares that occurred on 2010 October 29 and 2011 January 2. Both flares show loop-shaped SXR sources in the time intervals close to the GOES peak times. We deliberately avoided the hard X-ray peak so that the X-ray emission in the selected time intervals during the decay phase is mostly thermal. RHESSI detected no enhanced emission above 25 keV and the attenuator state was at A0 (highest sensitivity at low-energy X-rays) during the two flares. Figure 1 depicts the light curves of the two events and the time intervals used in this study.

3.2. Observations

Figures 2 and 3 show the RHESSI images reconstructed by all the algorithms and 131 Å images taken by Solar Dynamics Observatory (SDO)/AIA. We used detectors 3–6, 8, 9 and an image size of 129 × 129 pixels with a pixel size of 1″. The CLEAN process was performed according to the approach described in Dennis & Tolbert (2019). The maximum iterations were set to 2000, CLEAN_beam_width_factor (CBWF) was set to 2.0, and the scaled_resid was used for the CLEAN_regress_combine_method. Other parameters were set to the RHESSI defaults.

The X-ray source in the first flare (Figure 2) appears to be a narrow loop. Most algorithms produce consistent results in general, but the FF image is clearly different, which displayed a source with wrong orientation and size of the loop, despite that a seven-parameter loop model was used. The VF image exhibits a tendency for breaking up and discontinuity in the source. The lengths of the loops presented by different algorithms are relatively consistent, while there is considerable variation in the widths of the loop. This may be attributed to the inadequate measurement of the smallest dimensions of the sources, similar to Dennis & Pernak (2009).

The CLEAN image shows a wider loop-shaped source than the input source (which may be corresponding to the CBWF and detectors we used). The PIXON, EM, MEM_GE and VIS_WV images present more or less consistent results. The width of the loop source in the MEM_NJIT image is small and similar to that in the AIA 131 Å image, showcasing its superior ability to image narrow sources, as demonstrated in Dennis & Pernak (2009), Warmuth & Mann (2013), Dennis & Tolbert (2019). The VIS_CS image presents a wide loop with two bright sources near the loop top. The UV_Smooth image is also a wide loop with obvious sidelobes, exactly as depicted in Massone et al. (2009). Although the VF image shows a nice loop structure, the shape of the loop is different from the observation. It is mainly due to the fact that irregular loop

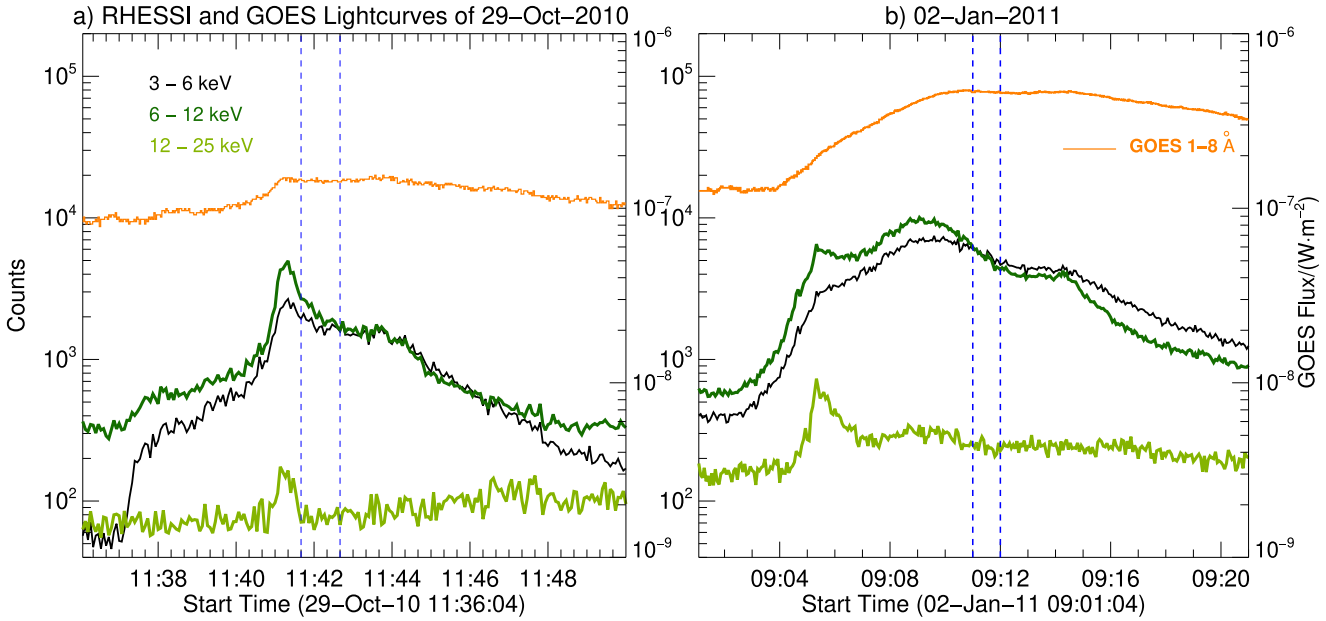

Figure 1. RHESSI and GOES light curves of the two GOES B-class flares. The blue vertical lines indicate the one-minute integration time for imaging. Left panel: the GOES B1.4 flare from 2010 October 29 11:37:16 to 11:50:32 UT, located in the active region AR 11117. Right panel: B4.6 flare from 2011 January 2 09:00:44 to 09:25:56 UT in AR 11140.

shapes cannot be reconstructed with the loop models used in the current VF method.

Figure 3 shows another example of a larger loop, with more scattered emissions around. The situation in this case is similar to that in the first flare. FF exhibits the same problems and its Cstat and reduced χ^2 have fairly high values of 6.625 and 18.881 respectively, while those of other algorithms are all less than 2.6, as shown in Table 1.

3.3. DEM-X Images from AIA DEM Maps

Comparing and evaluating images obtained by different algorithms can be challenging when the true properties of the source are unknown. In most simulation studies, input images are a combination of assumed sources that have certain simple shapes. However, in observational cases, the ground truth is usually missing. To solve this problem and use more realistic HXR sources as input images, we computed low-energy thermal X-ray images from EUV observations of SDO/AIA as ground truth.

First we obtain DEM maps of thermal plasma from SDO/AIA data. The EUV images taken by the six AIA channels (94, 131, 171, 193, 211, and 335 Å) are processed to level 1.5 using the standard AIA procedure aia_prep.pro. We average AIA images during the RHESSI integration time and rebin the images by 2×2 pixels, resulting in a pixel size of $1\farcs2$. Second, we calculate thermal bremsstrahlung X-ray maps in the ranges of 4–10 keV and 15–20 keV from the DEM maps using f_vth.pro provided by Solar SoftWare (SSW). These SXR maps are then compared with the imaging results of RHESSI and HXI, and used in imaging simulations for the test of algorithms.

The calculated DEM-X 4–10 keV images are shown on the top left of Figures 4 and 5. The consistency between the DEM-X image and the one obtained from RHESSI is good in general, but there are differences in detailed structure, as expected. It is known that indirect imaging from limited modulation profiles or visibilities cannot reconstruct all details, and its dynamic range cannot compete with that of direct imaging.

The DEM-X image for the test of HXI is obtained in the energy range of 15–20 keV because the starting energy for imaging with HXI is about 15 keV (Su et al. 2024), much higher than that of RHESSI at 3 keV. The possibility of contribution from non-thermal emission is also higher, making it difficult to compare the image with the thermal X-ray image from DEM. Besides, thermal emission in 15–20 keV often originates from hot plasma at temperatures greater than 20 MK (or hot plasma with lower temperatures but high emission measure), which is beyond the most sensitive range of AIA temperature responses. However, the results of such a test are still useful.

4. Imaging Simulation with RHESSI Software

Using the simulation mode of RHESSI software (Schwartz et al. 2002), we tested ten imaging algorithms in four cases. The first is a test with input sources from the AIA-based 4–10 keV images; the second one is a test of flux ratios of double Gaussian sources with equal fluxes. The third one is a

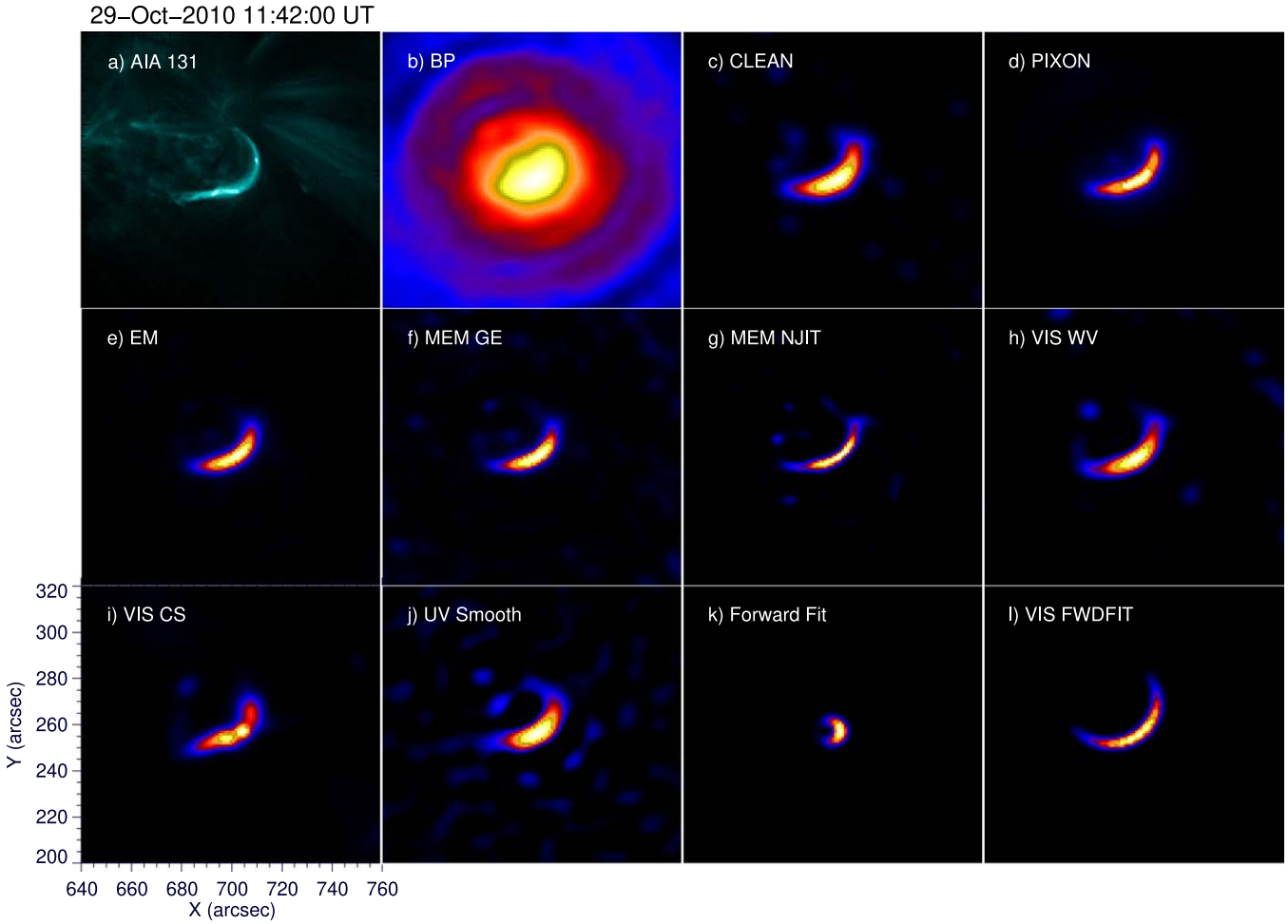

Figure 2. AIA and RHESSI images of the flare observed on 2010 October 29. Top left panel: AIA 131 Å image taken at 2010 October 29 11:42:00 UT. Other panels: RHESSI 4–10 keV images of all algorithms, reconstructed for 11:41:40–11:42:40 with 3–6, 8, 9 F. Natural weighting was used for CLEAN and BP. The images consist of 129 × 129 pixels with a pixel size of 1″. Except for CLEAN, FF and VF, the settings of the algorithms are RHESSI defaults.

test of imaging dynamic range with double Gaussian sources that have different fluxes. The last case is a test of CLEAN beam size with a single Gaussian source in different sizes. We implemented the simulation process in https://hesperia.gsfc.nasa.gov/rhessi3/software/simulation-software/index.html.

4.1. Case 1: Simulation with Realistic Sources

In this simulation test, we adopted the same pointing and imaging center from the observations. The pixel size is set to 1.″2 (same as that of the rebinned AIA maps), and the imaging FOV is 120″ × 120″. Other parameters are consistent.

Figure 4 shows the simulation results based on the 4–10 keV DEM-X image of the 2010 October 29 flare, which are in good agreement with those directly reconstructed from observations in Figure 2. The incorrect FF image remains unchanged. The super-resolution of MEM_NJIT makes it the closest approximation to the model. EM, PIXON, and MEM_GE perform well. The shape of the VIS_CS source is not quite consistent with that in the input image, and other algorithms present relatively wide loops. According to the quantitative results of imaging quality (Table 2(a)), i.e., QuIX, Cstat and χ^2, the best two results in this case are from PIXON and EM, and the (relatively) worst two results are from FF and UV_Smooth.

The simulation results for the 2011 January 2 flare are also in good agreement with observations (except for the FF image in Figure 3). The AIA DEM-X 4–10 keV source in this case is a loop which is wide at the top and narrow at the legs. All the methods except FF produced the loop-shaped source, but some images show clear sidelobes. According to the quantitative results in Table 2(b), the best two results in this case are also from PIXON and EM, the same as those in the first case. All three indices suggest that the relatively bad three images are from FF, MEM_NJIT, and UV_Smooth. MEM_NJIT is not

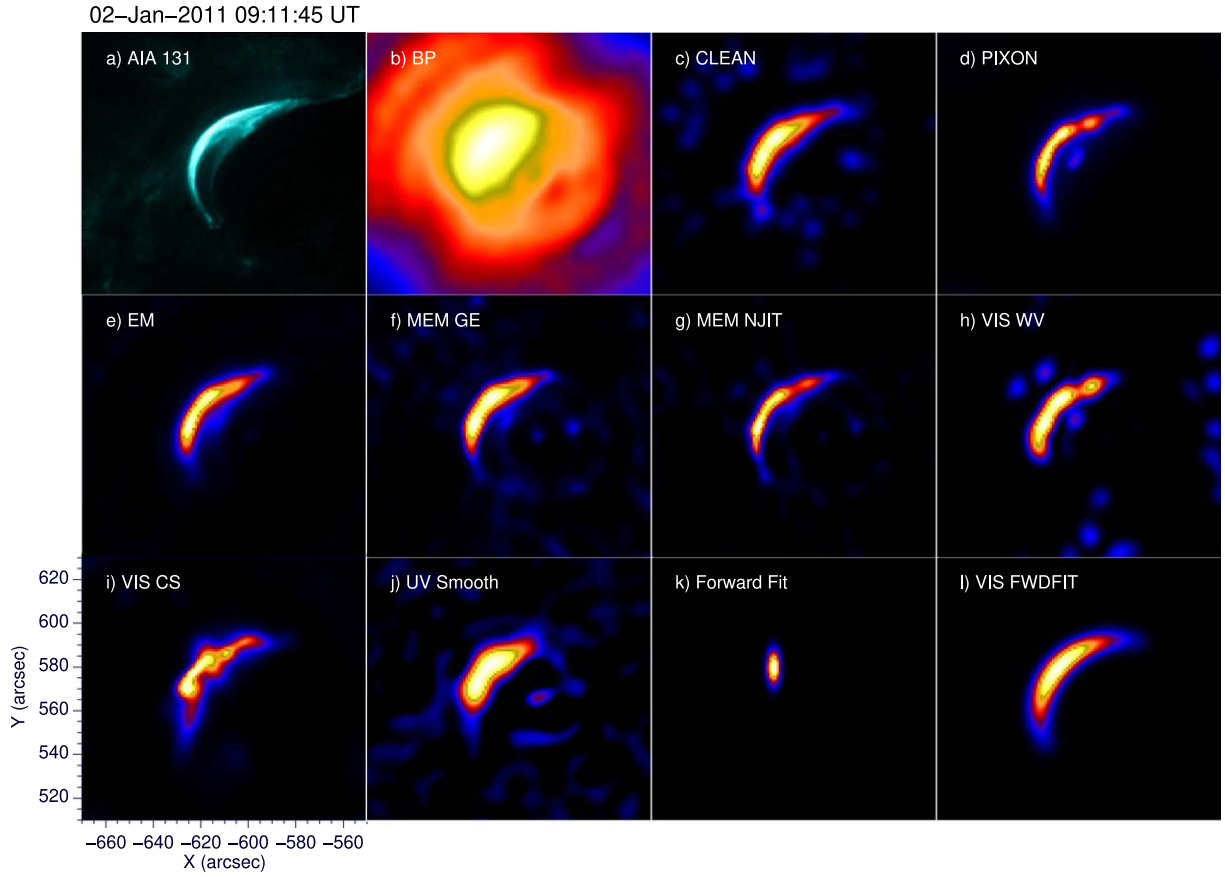

Figure 3. AIA and RHESSI images of the flare observed on 2011 January 2. RHESSI images are made for 09:11:00–09:12:00 in 4–10 keV. Other settings are the same as in Figure 2.

Table 1
Cstat and χ^2 of the Results in Figures 2 and 3

Event	Index	CLEAN	EM	PIXON	FF	VF	MEM_GE	MEM_NJIT	UV_Smooth	VIS_CS	VIS_WV
Figure 2	Cstat	1.258	1.219	1.234	2.158	1.298	4.817	1.153	5.109	1.243	5.162
	χ^2	1.21	1.33	1.49	8.71	1.2	2.41	1.15	4.02	1.34	2.54
Figure 3	Cstat	2.548	2.146	2.144	6.625	1.687	1.658	1.432	2.366	1.298	1.651
	χ^2	1.39	1.279	1.228	18.881	1.328	1.292	1.296	1.664	1.256	1.567

performing as well as in Table 2(a), probably due to the super-resolution effect of MEM_NJIT, resulting in a smaller source size and different flux distribution along the loop compared to the source.

In Table 2, Cstat, χ^2 and QuIX are consistent in most cases. It appears that Cstat overestimates the performance of VIS_CS, and QuIX overestimates the performance of FF (Table 2(a)). But overall, QuIX is an effective supplement to χ^2 and Cstat, particularly in assessing sidelobes. Using all three parameters together can help verify image quality and provide a comprehensive evaluation of the imaging results.

4.2. Case 2: Double Sources with Equal Fluxes

In this test, we evaluate the performance of the algorithms using double Gaussian sources with the same flux but different sizes. Accurate flux ratios of the two sources in reconstructed images are important for investigations of HXR imaging spectroscopy and understanding of the particle acceleration/transport process.

As shown in Figure 8 of Felix et al. (2017), simulated detector count statistics can impact image morphologies. Here, we used two different signal-to-noise ratios (SNRs) by changing the background intensity and the statistical level

Table 2
Comparisons of Cstat, reduced χ^2 and QuIX for the Imaging Results (Figures 4 and 5) of the Simulation Test Based on AIA DEM-X 4–10 keV Images

		CLEAN	MEM_GE	MEM_NJIT	VIS_CS	VIS_WV	UV_Smooth	EM	PIXON	VF	FF
(a)	QuIX	0.864	0.904	0.909	0.892	0.896	0.835	0.916	0.907	0.906	0.872
Figure 4	Cstat	1.052	1.025	1.054	1.007	1.097	2.967	1.002	0.988	1.877	4.202
	χ^2	1.674	1.607	1.098	1.350	1.568	1.741	1.013	0.928	1.512	13.98
(b)	QuIX	0.845	0.784	0.757	0.835	0.805	0.745	0.850	0.853	0.832	0.744
Figure 5	Cstat	1.057	1.172	1.265	1.025	1.225	1.743	1.024	1.015	1.115	4.591
	χ^2	1.291	1.500	1.959	1.205	1.480	1.526	1.057	1.021	1.149	17.045

Note. The text in blue indicates the best three images revealed by the corresponding index, and the text in magenta indicates the relatively worst three images.

Table 3
Source Parameters of the Results in Figure 6

SNR[a]	Algorithms	Model	CLEAN	MEM_GE	MEM_NJIT	VIS_CS	VIS_WV	UV_Smooth	EM	PIXON	VF[c]	FF
	Flux ratio	1.0	0.959	0.862	0.852	0.893	0.903	0.832	0.858	0.859	0.980 ± 0.029	0.554
	P_{bk}	0	0.120	0.345	0.248	0.114	0.395	0.352	0.272	0.214	0.059 ± 0.014	0.078
30	Source 1	FWHM =11.8	11.085	8.220	8.570	9.869	9.369	9.578	7.689	8.143	8.983 ± 0.32	6.183
	Source 2	7.1	9.014	6.901	6.341	7.697	6.991	9.380	6.308	7.247	10.404 ± 0.22	5.415
	Cstat		1.115	1.171	1.104	1.029	1.457	6.693	1.052	1.035	1.385	1.416
	χ^2		1.93	1.92	1.67	0.99	2.61	2.97	1.06	0.97	3.0	2.66
	QuIX	1.000	0.943	0.946	0.977	0.977	0.918	0.843	0.974	0.947	0.915	0.951
	Flux ratio	1.0	1.270	1.140	0.998	1.083	1.284	1.234	0.967	1.188	1.097 ± 0.24	0.607
	P_{bk}	0	0.289	0.451	0.481	0.247	0.471	0.606	0.369	0.302	0.177 ± 0.085	0.086
5	Source 1	FWHM =11.8	12.797	11.821	11.430	13.059	11.851	14.268	9.898	12.299	12.598 ± 3.08	6.576
	Source 2	7.1	7.892	5.470	5.186	7.504	6.318	8.768	5.554	7.757	5.826 ± 0.99	5.365
	Cstat		1·117	1.143	1.154	1.115	1.280	3.183	1.114	1.120	1.112	1.132
	χ^2		0.947	0.870	0.944	0.995	0.959	1.659	0.995	1.020	1.013	1.141
	QuIX	1.000	0.928	0.910	0.922	0.942	0.887	0.751	0.955	0.937	0.966	0.951

Notes. The Best Three Images According to the Corresponding Parameters or Indices are Marked in Blue.
[a] SNR_value, a RHESSI imaging parameter, is the value of SNR computed from visibilities.
[b] The source flux and size are both calculated at the 5% contour level. The source size was obtained from the IDL procedure HSI_GET_EXTENT.pro.
[c] Errors are derived from the VF 1σ uncertainty.

(counts per detector) during the simulation process. To ensure the consistency between simulation and observation, we employed the snr_value[4] defined in the RHESSI program to specify the SNR and provide an approximate SNR value in Table 3.

Figure 6 displays the test result for SNR = 30, which is roughly comparable to the observational SNR in Figure 2, effectively illustrating the sizes and fluxes of the sources. In this case, the left source (Source 1) is slightly larger than the right one (Source 2), with respective Gaussian full width at half maximum (FWHM) values of 11.″8 and 7.″1. The UV_Smooth image has obvious sidelobes, which are similar to the previous results. VIS_WV exhibits nonexistent structures at the edge of the imaging area. In the PIXON image, there is an additional weak source on the upper left of Source 1.

The source parameters are presented in Table 3, where the sizes and fluxes of the two sources are obtained within 5% contour level. The flux ratios of Source 1 and Source 2 are consistent within the 17% range of the assumption of 1 for all the methods except FF, which is nearly half of the flux ratio in

[4] https://hesperia.gsfc.nasa.gov/ssw/hessi/doc/params/snr_chk_doc.htm

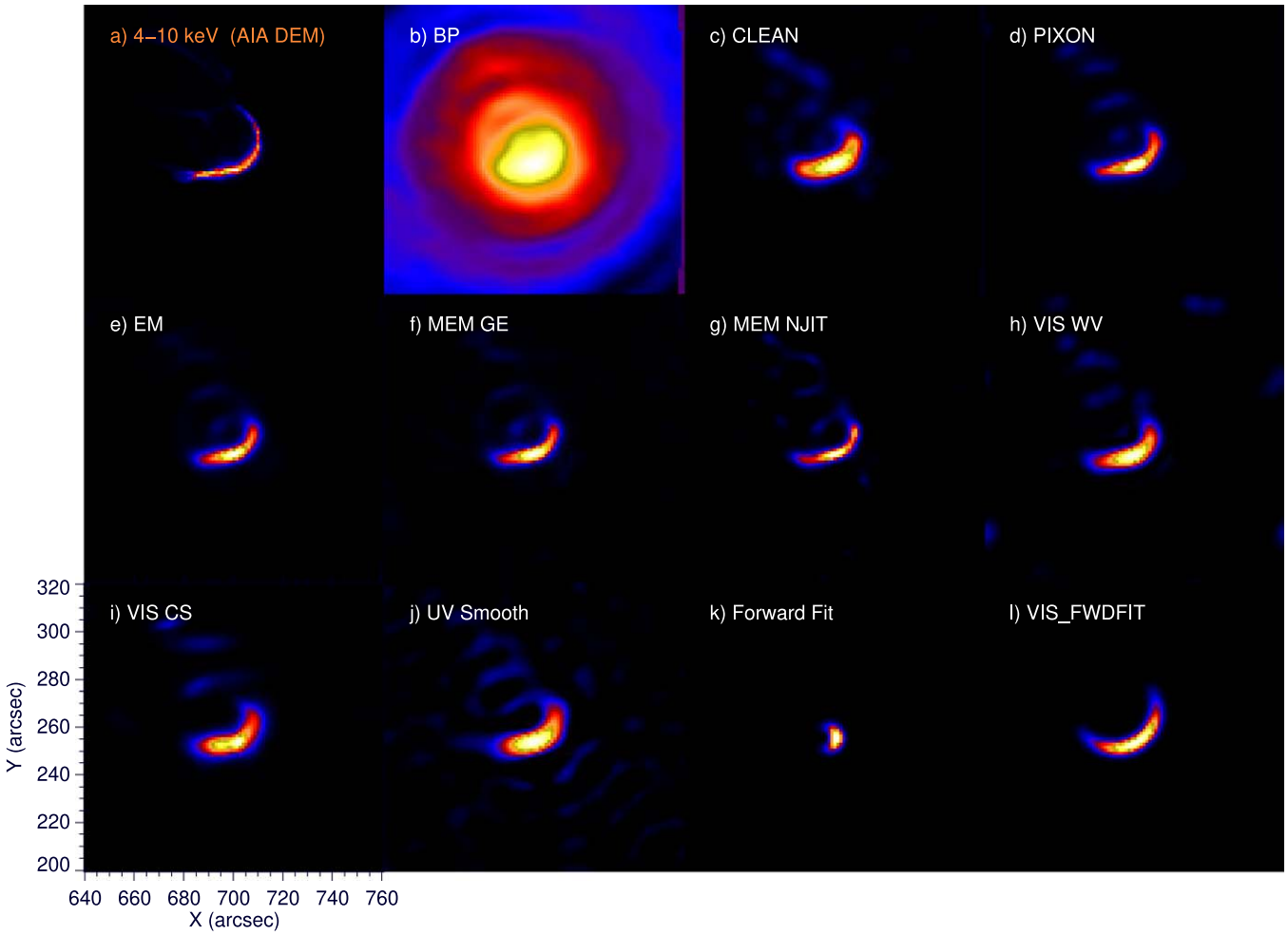

Figure 4. The 4–10 keV image calculated from DEM maps for the 2010 October 29 flare and the corresponding images reconstructed by all the algorithms through RHESSI simulation. The same aspect solution and imaging center as those in Figure 2 are used. The pixel size is 1.″2 and the image size is 120 × 120 arcsec^2.

the model. The proportion of the background flux is calculated from the source flux and total flux, $P_{bk} = \frac{F_{\rm total} - F_{\rm sources}}{F_{\rm total}}$. As shown in Table 3, the two forward fit images have the lowest background. CLEAN and VIS_CS also have low background, followed by PIXON, MEM_NJIT, and EM. The backgrounds of MEM_GE, VIS_WV, and UV_Smooth are the strongest. It should be pointed out that the emissions below 5% around the source are considered as background here, which may result in a smaller source flux and a corresponding larger background. Sidelobes that are close to the sources may contribute in the source flux, resulting in a larger source flux.

The VF image fails to accurately obtain the sizes of the two sources, and Source 1 is smaller and brighter than Source 2, which is opposite to the model. Both sources of FF are smaller than those in the model. Overall, the deviation in the size ratio between the images and the model is significant, while the flux ratio remains acceptable for most methods.

For the test with SNR = 5 (Figure 7), the overall image quality clearly decreased and sidelobes increased, which also impacts the topological morphology of one of the two main sources. Quantitatively, the larger source (Source 1) is mixed with the surrounding background, resulting in a higher flux ratio, and the total background flux P_{bk} noticeably increases. The P_{bk} of VIS_CS remains at a low level across different SNRs, ranking just below VF and FF. This confirms the accurate and robust photometry of VIS_CS (Felix et al. 2017). The sizes of Source 1 are larger than those in the case of SNR = 30 (except for FF), and the sizes of Source 2 are less affected by the SNR compared to Source 1. No significant differences are found in Cstat for most methods. χ^2, however, significantly decreased, which cannot represent the decreasing image quality. The QuIX decreased for all the methods except VF and FF, which successfully reflects the decrease in image quality. The SNR has a considerable impact on the flux measurements. From the uncertainties provided by the VF

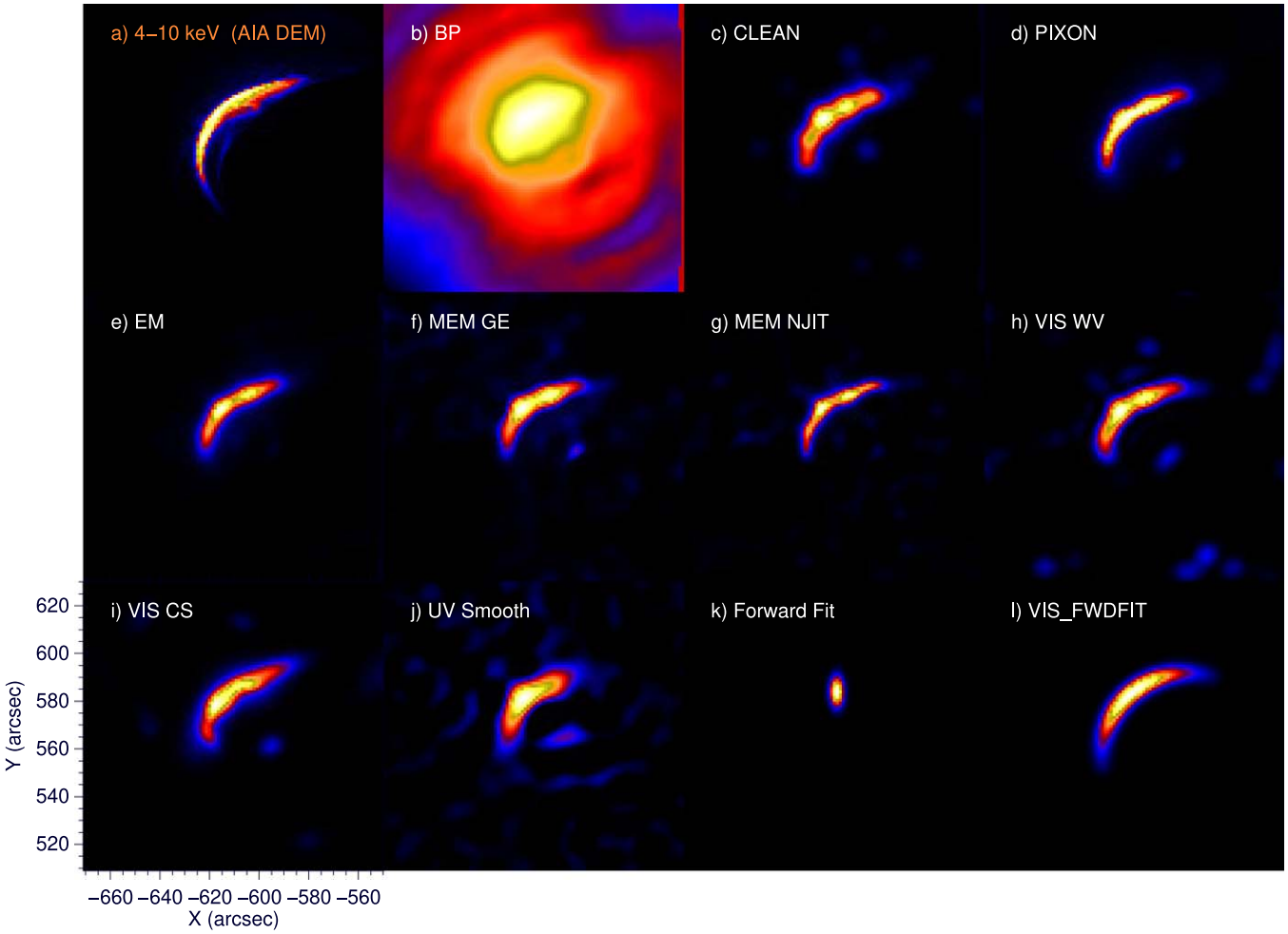

Figure 5. Same as 4 but for 2011 January 2 flare. The white arrow points to the weak source under the loop.

algorithm, it is evident that the errors significantly increase when SNR is 5. Although all algorithms are affected by the SNR of 5 to some extent, they generally maintain a good level of robustness. Changes in SNR do not significantly alter the conclusions drawn about the algorithms.

4.3. Case 3: Imaging Dynamic Range

The design goal of RHESSI is to achieve a dynamic range of 100:1 when there are sufficient observational counts (Hurford et al. 2002). In practical observations, the dynamic range is influenced by various observational conditions, resulting in varying outcomes. Nonetheless, a dynamic range of 10:1 is typically achievable (Piana et al. 2022). To test the imaging dynamic ranges of the algorithms, we simulated a series of double-source scenarios, where both sources have the same size but different intensities.

First, we investigate the imaging dynamic range using simulated double Gaussian sources with the same FWHM (8.″2) but varying fluxes. The flux ratio R_{12} of the weak source (Source 1) and the strong source (Source 2) ranges from 0.1 to 0.9, and no background was added in the simulations. Figure 8 shows examples of the models with different R_{12} (left column) and the corresponding images generated by three algorithms (the three columns on the right). For $R_{12} = 0.2$, the weak source is not clearly visible in the EM image; however, it appears more pronounced in the MEM_GE and UV_Smooth images.

To compare the flux ratio R_{12} of two sources in the imaging results, we first used the 5% contour of the maximum intensity to obtain the flux of each source. However, if the weaker source is below the 5% threshold, this approach seems to limit the identification of the weaker sources. The second method searched for the strongest intensity around the known position of the source to represent the peak intensity. The results of the

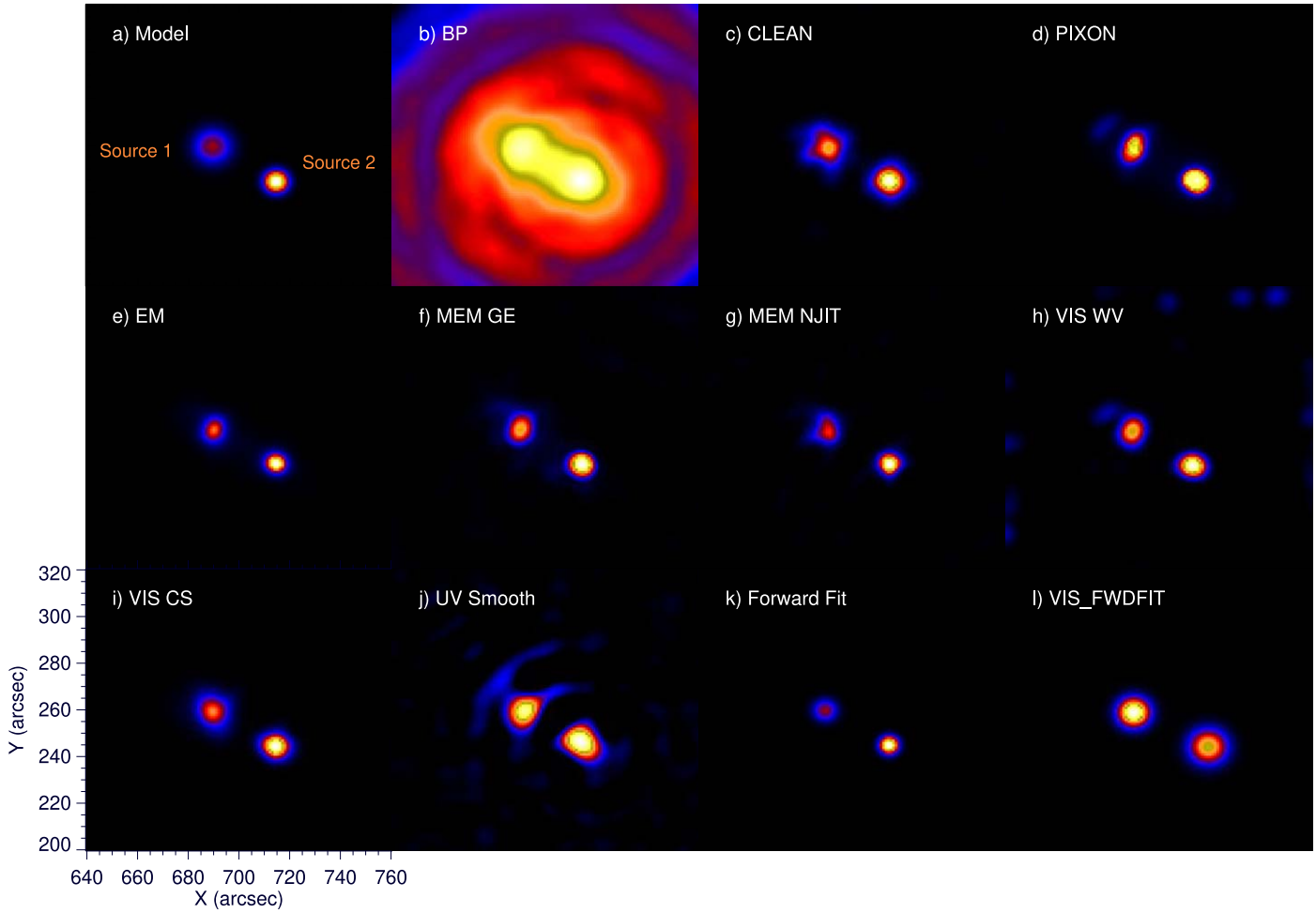

Figure 6. Simulation results for the case with two sources of same total flux. The FOV is 120 × 120 arcsec^2. (a) Input models with two Gaussian sources. Source 1 is larger with its FWHM of 11.″8. The other one has a size of 7.″1. Other panels: images reconstructed by the algorithms. Aspect solution and imaging center of Figures 2 are used. Other settings are the same as the previous figures.

two methods are shown in Table 4, which shows the R_{12} of the model and the images. Most algorithms exhibit an R_{12} smaller than the model as expected.

In Table 4, FF deviates from the model, reflecting substandard flux allocation, with the flux ratios notably smaller than those in the model. When the R_{12} of the model is equal to 0.1, EM and UV_Smooth cannot identify the weak source. At $R_{12} = 0.2$, EM is still unsatisfactory, for which the super-resolution effect may be responsible. EM results become better with the increase of R_{12}, and are comparable to other algorithms. The weak sources in all the MEM_GE images are relatively weaker than the model, but it can be barely identified at $R_{12} = 0.1$. MEM_NJIT consistently outperforms MEM_GE in terms of R_{12}, which is expected as it is considered to be excellent for determining component fluxes (Schmahl et al. 2007).

The weak sources and sidelobes are mixed together in the UV_Smooth images, resulting in larger intensities in the weak sources and higher flux ratios compared to the model. At $R_{12} = 0.9$, some algorithms also show slightly higher flux ratios than the model, possibly due to a similar reason. Overall, VF is the closest to the model, primarily because both the method and the model do not include any background flux, and the number of sources is known.

Other algorithms perform almost equally well in most cases. The dynamic range of distinguishable sources can reach 10:1 in this simulation. However, various backgrounds in the actual observations will bring more uncertainties.

In addition, we also tested the imaging dynamic range with two point sources. Here, R_{12} varies from 0.1 to 0.9. Notably, no background was incorporated into these simulations. The same statistically low-level condition comparable to a B-class flare was employed as in previous tests. Figure 9 shows examples of the models with different R_{12} (left column) and the corresponding images generated by three algorithms (the three columns on the right).

Table 4
Flux Ratio R_{12} of the Two Gaussian Sources in the Models and Reconstructed Images Corresponding to Figure 8

Flux	R_{12}	CLEAN	MEM_GE	MEM_NJIT	VIS_CS	VIS_WV	UV_Smooth	EM	PIXON	VF	FF
	0.1	0.027	0.0045	0.010	0.003	0.029	0.067	0.0	0.008	0.055	0.017
	0.2	0.128	0.047	0.075	0.085	0.115	0.160	0.001	0.126	0.165	0.068
Total	0.3	0.262	0.152	0.225	0.256	0.236	0.313	0.184	0.253	0.278	0.136
	0.4	0.353	0.246	0.324	0.347	0.314	0.405	0.280	0.369	0.374	0.205
	0.5	0.472	0.352	0.429	0.455	0.425	0.539	0.402	0.439	0.470	0.296
	0.6	0.566	0.483	0.554	0.561	0.533	0.653	0.507	0.525	0.585	0.381
	0.7	0.671	0.573	0.652	0.645	0.635	0.719	0.617	0.673	0.682	0.432
	0.8	0.761	0.683	0.765	0.755	0.752	0.818	0.718	0.764	0.764	0.489
	0.9	0.901	0.813	0.898	0.942	0.875	0.953	0.871	0.849	0.889	0.544
	0.1	0.085	0.030	0.064	0.041	0.091	0.070	0.0	0.061	0.102	0.062
	0.2	0.134	0.122	0.138	0.149	0.206	0.148	0.031	0.176	0.155	0.103
Peak	0.3	0.243	0.239	0.214	0.192	0.328	0.255	0.211	0.252	0.247	0.147
	0.4	0.332	0.332	0.358	0.300	0.406	0.317	0.321	0.384	0.352	0.178
	0.5	0.458	0.460	0.558	0.482	0.511	0.381	0.469	0.466	0.467	0.228
	0.6	0.581	0.600	0.764	0.578	0.646	0.509	0.598	0.580	0.679	0.275
	0.7	0.676	0.694	0.846	0.938	0.710	0.578	0.696	0.758	0.708	0.320
	0.8	0.758	0.789	0.931	0.793	0.756	0.655	0.799	0.912	0.773	0.343
	0.9	0.883	0.891	0.932	0.676	0.808	0.662	0.892	0.790	0.902	0.473

Table 5
Same as Table 4 but for the Case of Single-pixel Point Source

Flux	R_{12}	CLEAN	MEM_GE	MEM_NJIT	VIS_CS	VIS_WV	UV_Smooth	EM	PIXON	VF	FF
	0.1	0.055	0.008	0.052	0.017	0.014	0.052	0.006	0.011	0.108	0
	0.2	0.136	0.031	0.130	0.111	0.118	0.183	0.120	0.165	0.207	0.012
Total	0.3	0.269	0.158	0.275	0.235	0.237	0.282	0.242	0.300	0.322	0.259
	0.4	0.346	0.243	0.333	0.331	0.332	0.405	0.336	0.380	0.404	0.331
	0.5	0.482	0.364	0.486	0.444	0.439	0.503	0.461	0.467	0.510	0.425
	0.6	0.615	0.522	0.605	0.603	0.581	0.594	0.587	0.619	0.639	0.548
	0.7	0.663	0.604	0.684	0.662	0.647	0.660	0.661	0.684	0.713	0.605
	0.8	0.766	0.717	0.786	0.766	0.742	0.790	0.754	0.768	0.806	0.689
	0.9	0.867	0.830	0.908	0.873	0.838	0.874	0.855	0.858	0.898	0.744
	0.1	0.081	0.014	0.058	0.036	0.043	0.098	0.022	0.014	0.250	0.001
	0.2	0.178	0.067	0.174	0.128	0.152	0.165	0.121	0.285	0.129	0.092
Peak	0.3	0.301	0.179	0.304	0.233	0.255	0.241	0.220	0.394	0.164	0.286
	0.4	0.377	0.262	0.279	0.332	0.341	0.297	0.293	0.540	0.201	0.364
	0.5	0.495	0.398	0.415	0.415	0.470	0.354	0.387	0.557	0.285	0.436
	0.6	0.624	0.557	0.590	0.373	0.603	0.435	0.508	0.664	0.346	0.561
	0.7	0.683	0.656	0.732	0.724	0.683	0.481	0.634	0.863	0.420	0.582
	0.8	0.775	0.728	0.684	0.726	0.748	0.549	0.701	0.802	0.366	0.642
	0.9	0.872	0.838	0.806	0.862	0.825	0.604	0.809	0.957	0.423	0.691

Note. The footpoint flux ratios R_{12} are for the models and the reconstructed images corresponding to Figure 9.

Table 5 presents the flux ratios and the peak intensity ratios. Both yield broadly comparable results. However, at $R_{12} = 0.1$, the flux of the weak source is significantly underestimated in all methods except VF. FF even fails to identify the weaker source. The peak intensity results are slightly better, but only UV_Smooth and CLEAN produce consistent ratios with the model within a 20% range. Conversely, at $R_{12} = 0.9$, the threshold effect introduced by the 5% contour is less pronounced, and the flux ratio is more consistent with the model R_{12}. The peak intensity ratios obtained from VF, UV_Smooth, and FF are clearly different from the input. For instance, VF should theoretically increase continuously with the input ratio. However, the actual results exhibit erratic fluctuations instead.

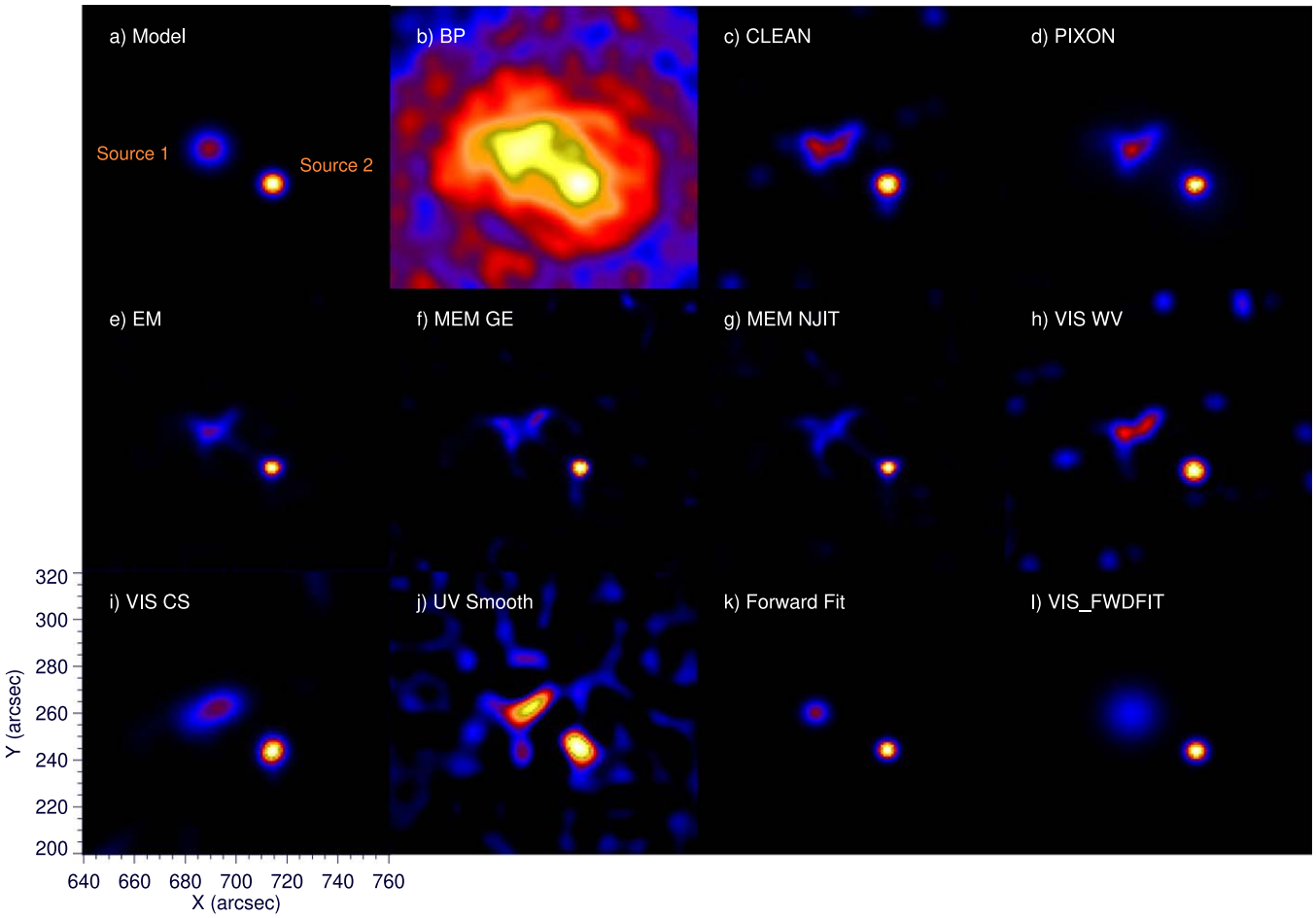

Figure 7. Same as Figure 6 but for the case with SNR of 5.

Overall, most methods produce good results for source fluxes. Among them, VF provides the most accurate estimate of the source fluxes. FF, however, does not provide a consistent result with the input. The differences among the algorithms at various R_{12} values are relatively minor, and most methods achieve a dynamic range of 10:1 (the weak source can be identified at the 5% contour).

4.4. Case 4: CLEAN Beam Size

There are a few parameters in the CLEAN algorithm, such as the max number of iterations, the method for combining the clean component map and residual map, CLEAN_beam_-width_factor (CBWF), etc. Among them, CBWF is an important free parameter that affects the CLEAN beam size and therefore source sizes, as well as imaging quality. According to the definition in RHESSI software, the width (σ) of the Gaussian source convolved with CLEAN components is related to the resolution of selected detectors (R_i), its weights (w_i) and CBWF,

$$\sigma = \frac{0.45}{\mathrm{CBWF}} \times \sqrt{\frac{\Sigma w_i}{\Sigma (w_i/R_i^2)}} \sim \frac{R_i}{\mathrm{CBWF}}. \quad (1)$$

When the default 1 of CBWF is used for imaging, sources often appear larger compared to those produced by other methods. Larger CBWF narrows the width of convolving Gaussian sources and produces smaller source sizes. Better imaging can be obtained by adjusting CBWF in many cases. Dennis & Tolbert (2019) performed imaging using CBWF values of 1, 2, and 10. The resulting Cstat remained unchanged, but the reduced χ^2 was improved significantly as CBWF increased. However, at CBWF = 10, the image approached that of the CLEAN component, with the sources appearing noticeably dispersed and fragmented. Kontar et al. (2010) found in a particular event that using 1.7 for CLEAN can produce images comparable to other algorithms, but it is still unknown what the universally appropriate value is. Here we

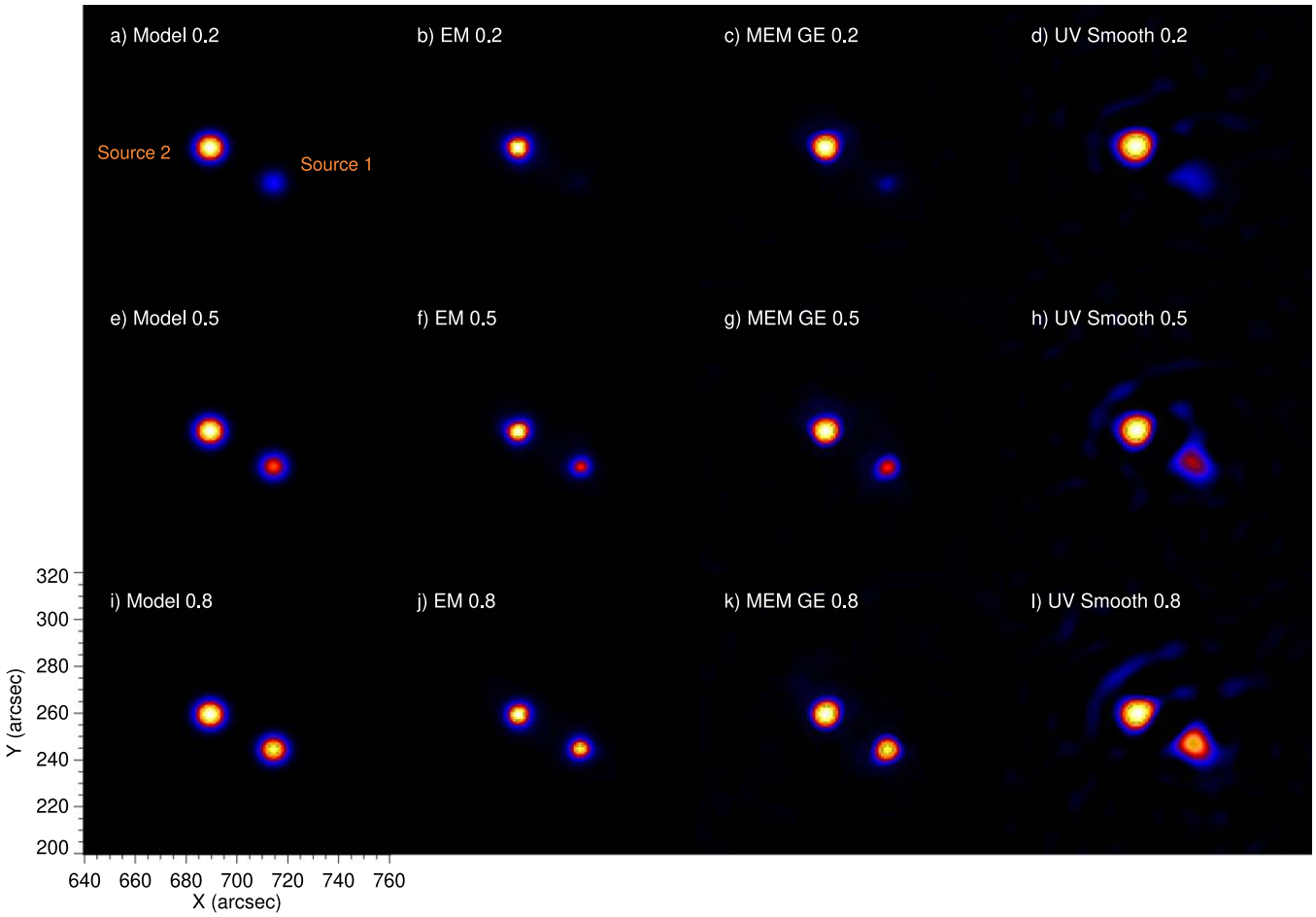

Figure 8. Simulation results for the case with two footpoint sources of different flux. The first column: Input models of two sources with different flux ratio. The flux and size of Source 2 remain unchanged in different models. Source 1 is variable, and the ratio of its flux to Source 2 (R_{12}) is 0.2, 0.5 and 0.8. The three columns on the right are the results of three imaging algorithms, and each row corresponds to the model on the left.

simulated a series of single Gaussian source with different widths to find the best default setting for CBWF.

For each width, we used different CBWF values (with a bin size of 0.1) and detector combinations for imaging. All images were compared with the model to obtain their imaging quality QuIX. Figure 10 shows some examples of the models and images, which reveal that the quality of reconstructed images depends not only on the setting of CBWF but also on the source sizes and detector resolution (detector combinations). Small CBWF can indeed result in better images for large sources. But for small sources, the images are better with larger CBWF.

Figure 11 shows the QuIX results of imaging quality for RHESSI. The brighter color means better quality. The abscissa is CBWF, and the ordinate represents the size of the source (Gaussian FWHM). Figure 11(a)–(e) presents the results of imaging with different starting detectors and shows roughly the same trend. For a certain detector combination, larger sources require smaller CBWF to produce better images, and vice versa. From this perspective, the best CBWF is variable.

Using a simulated source provides the advantage of knowing the actual size of the source. So in Figure 11(f), we selected the finest starting grids with an approximately suitable resolution for each size of source, and found that the best value of CBWF for all detector combinations (brightest region) is around 2.0–2.4. The smallest source requires a large CBWF for an extremely narrow CLEAN beam to produce images that are more consistent with the model. We exclude the result of the smallest source and calculate the average value of the best CBWF for FWHM $3\overset{''}{.}53$–$37\overset{''}{.}7$, which is about 2.20. Considering that the sparse grid resolution is not sensitive to the continuous change in source size, it is anticipated that the error will exceed the bin size 0.1. Combining the bin size with the standard deviation of the optimal CBWF value results in an error of 0.326.

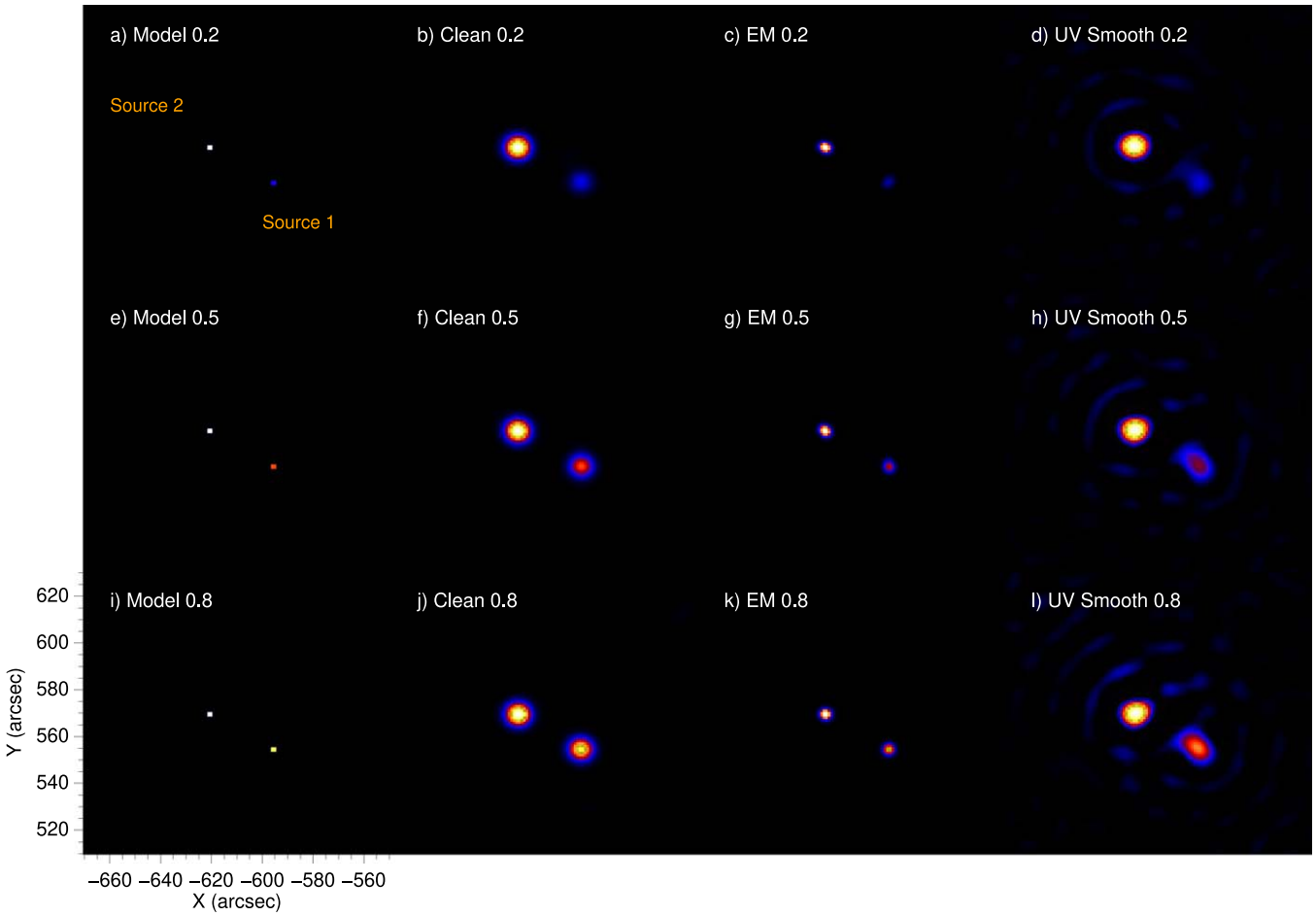

Figure 9. Simulation results for the case with two point sources of different flux. The flux and size of Source 2 remain unchanged in different models. The flux of source 1 is variable, and the flux ratio of R_{12} is 0.2, 0.5 and 0.8 for each row respectively.

Simply stated, when the appropriate detectors are selected, the fixed CBWF of 2.2 is sufficient. Therefore, we suggest a value of 2.2 as the default CBWF for RHESSI. However, to get the best image, one can further adjust the detector range and CBWF according to the source property.

5. Imaging Capabilities and Algorithms for HXI

5.1. HXI Observations

HXI has been observing flares for about two years, accumulating a substantial amount of observational data. Although the preliminary calibration result of HXI grids (G3–G10 groups) was released with HXI software, calibration of the finest grids (G1–G2 groups) for high-resolution imaging at low energies is still ongoing, which requires more data on compact flares. Furthermore, the visibility of HXI still requires more work on calibration (Su et al. 2024). Currently, there are five imaging algorithms available for HXI, including pattern-based HXI_BP, HXI_CLEAN, and Forward Fit, as well as visibility-based HXI_VIS_BP and HXI_VIS_CLEAN. Additionally, a machine learning based algorithm, HXI_DLA (Xia et al. 2024), is under development for practical use. Here in the following test, we reconstructed HXI images with basic calibration which takes into account the actual slit width and the grid shadowing effect.

Figure 12 displays the reconstruction results of a GOES M1.7 class flare observed by HXI on 2023 November 5. The images are reconstructed from grid groups G2–G10 in 35–50 keV. The sources in the HXI_CLEAN image correspond well with the AIA 1700 Å bright sources in Figure 12(f). The upper two sources are recognized as one large source by Forward Fit, and the VIS_CLEAN image also identifies them as an extended source, with the centroid between the two bright spots. In Forward Fit we assumed four Gaussian sources according to the HXI_CLEAN images, but found that the fourth source identified by FF is a faint source located to the right, which is also seen in Figure 12(b). For the current stage,

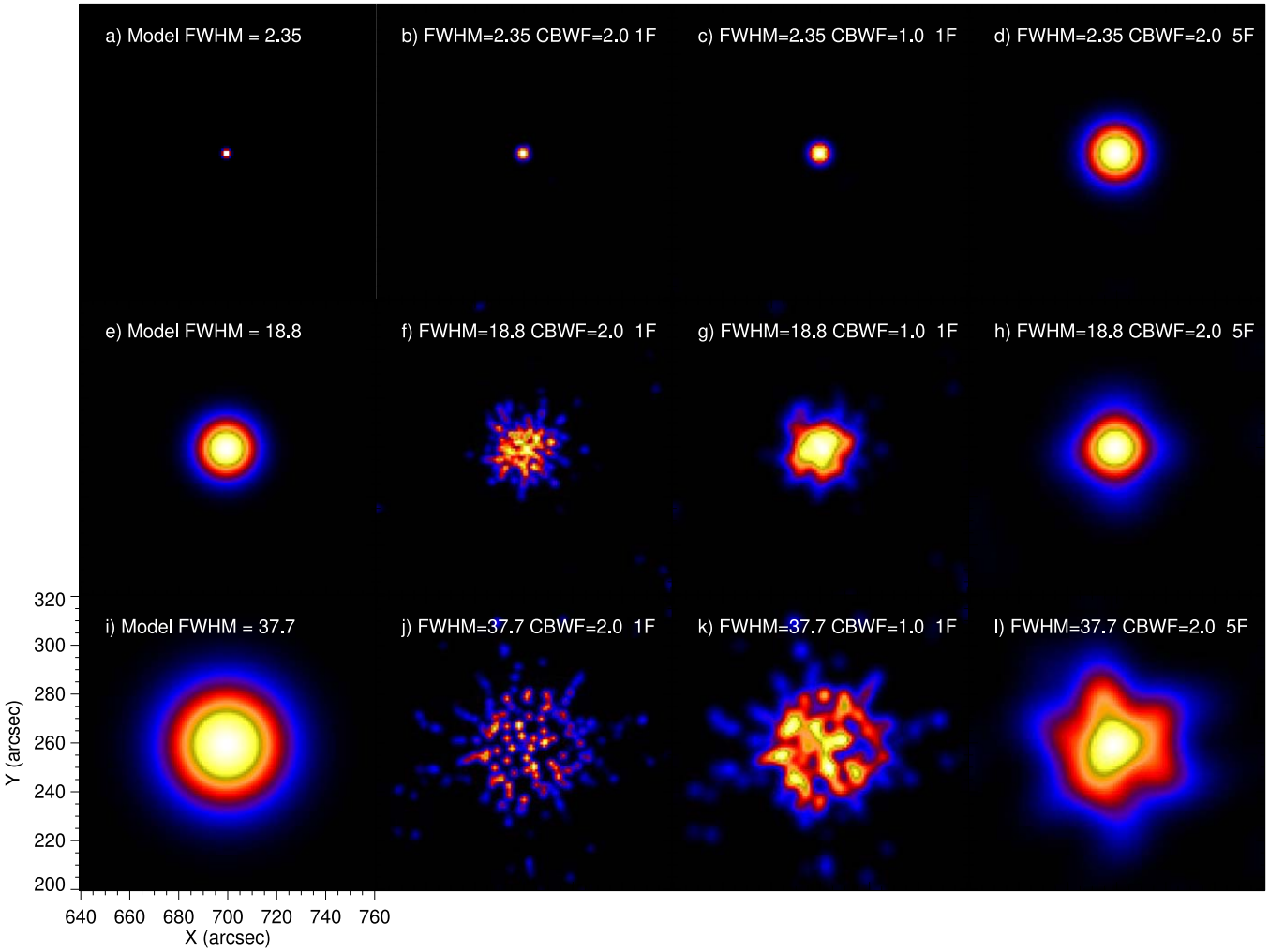

Figure 10. The simulation models and reconstructed CLEAN images in the CBWF test. Left column: Input models of a series of Gaussian sources with different sizes (Gaussian FWHM in arcsec). The three columns on the right are the CLEAN images reconstructed for the corresponding model with different parameters, the finest grids (detector resolution), and CBWF. The two columns in the center demonstrate that reducing the CBWF results in larger sources.

the HXI_CLEAN algorithm is recommended for scientific analysis.

5.2. DEM-X Test for HXI

In Figure 13, we tried to employ the AIA DEM-X method to test the imaging algorithms of HXI. Here we used the M5.0 flare data observed by HXI around 21:32:40 UT on 2023 March 5. As mentioned in Section 3.3, the AIA DEM calculation may not be accurate for thermal plasma at temperatures higher than 20 MK due to the low temperature response of AIA. Besides, there is a possible contribution from non-thermal emissions. These factors may cause the differences between the reconstructed image and the DEM-X image in 15–20 keV (Figure 13(a), (c)).

We used the DEM-X image as the simulation input for testing the algorithms. Figure 12(d)–(h) displays the images reconstructed from different algorithms. The HXI_CLEAN returns the best result, with a major source and two weak sources (indicated by the two magenta arrows), consistent with the input model. For HXI_VIS_BP and HXI_VIS_CLEAN we did not use G1–G3 groups which result in a resolution of $\sim 9\farcs3$ and the two weak sources are not identified.

5.3. Imaging Dynamic Range

In the following simulation, we tested the dynamic range of HXI with two footpoint sources similar to those in Figure 8, to assess its ability for identifying weak sources. We used two types of sources: Gaussian sources with FWHM $= 4\farcs7$ and point sources. Both tests were conducted under conditions of

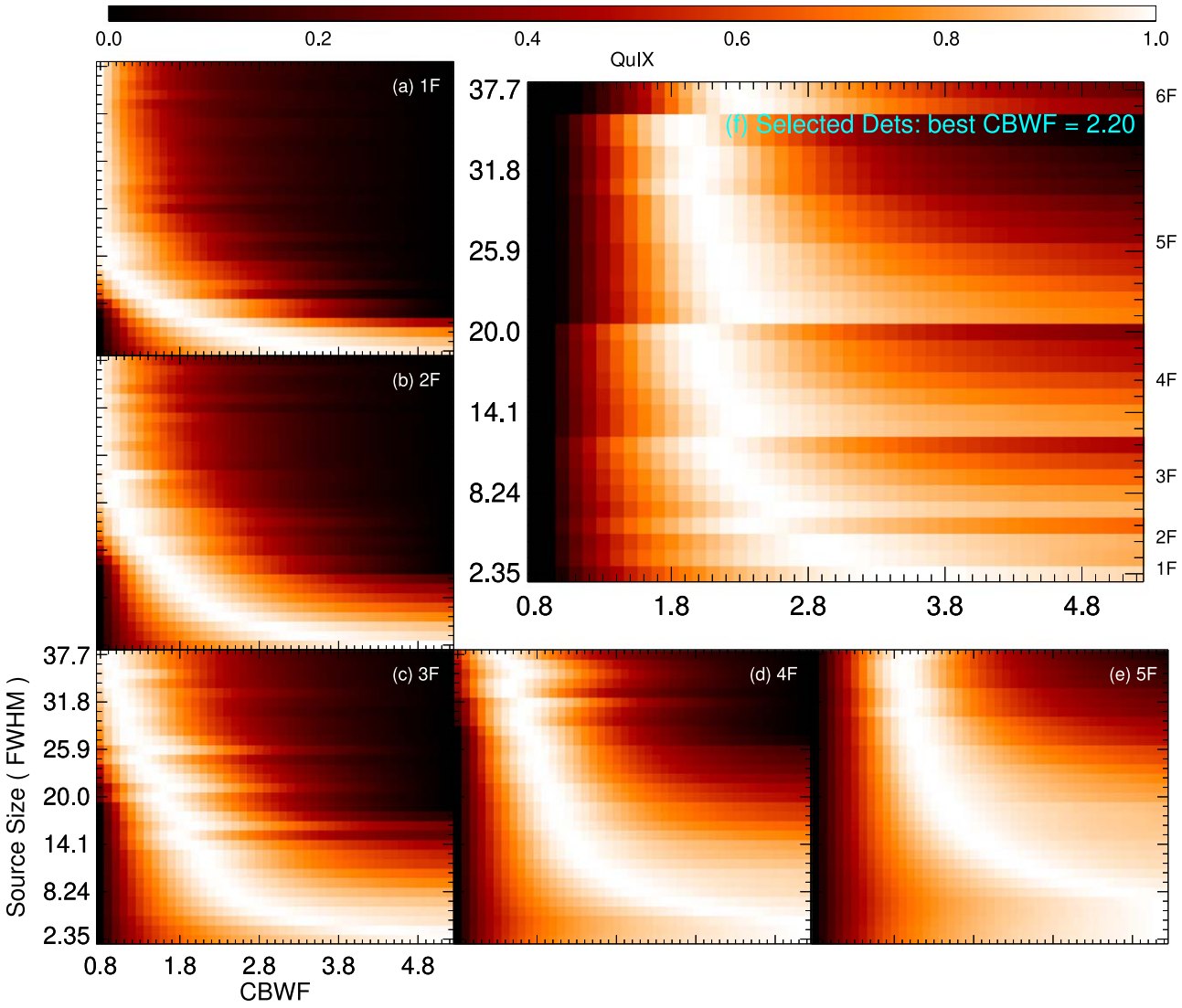

Figure 11. The QuIX results of the CBWF test for RHESSI. The brighter color means larger QuIX values and better images. The *X*-axis represents the CBWF value, and the *Y*-axis is the size of the Gaussian source (FWHM) in the model. Panels (a)–(e) are results with D1–D5 F as the finest subcollimator (starting detector for imaging) respectively. These panels show the same trend. For the same detector combination, larger sources require smaller CBWF for producing a good image, and vice versa. Coarser detectors require a larger CBWF to produce a source closer to the model. Panel (f) selects the detector combinations suitable for each of the source sizes and the best CBWF is found at around 2.0–2.4. The detector label on the right side of (f) shows the starting detector (finest grid) selected for the imaging of different source sizes.

high SNR and low background. The results for the Gaussian sources are presented in Figure 14, where two sidelobe sources are clearly visible. In Figure 14(c), with $R = 20$, the flux of the weak source is already less than that of the sidelobes, and the calculated flux ratio between the two sources at the 5% contour is nearly 207:1. (Note that we did not add a residual map in this study, which may improve the flux ratio. The method of adding a residual map to the cleaned map is another important topic of study.) Without additional evidence from actual observations, it is challenging to confirm the presence of a true source among the sidelobes. When $R = 30$, the weak source is completely unresolved. Therefore, the dynamic range of HXI is similar to that of RHESSI, approximately within the range of 10–20:1 (for imaging with G2–G10).

The results for the two point sources are shown in Figure 15 and Table 6. The faint source is barely visible at $R = 45$:1 and barely discernible at 50:1. The total flux ratio R (5% contour) and peak flux ratio suggest that HXI is capable of achieving a dynamic range of 50:1 in extreme cases (for imaging with G2–G10).

5.4. CLEAN Beam Size Test

In the HXI_CLEAN procedure, the width (σ) of the CLEAN beam is determined by the finest resolution of the grids selected

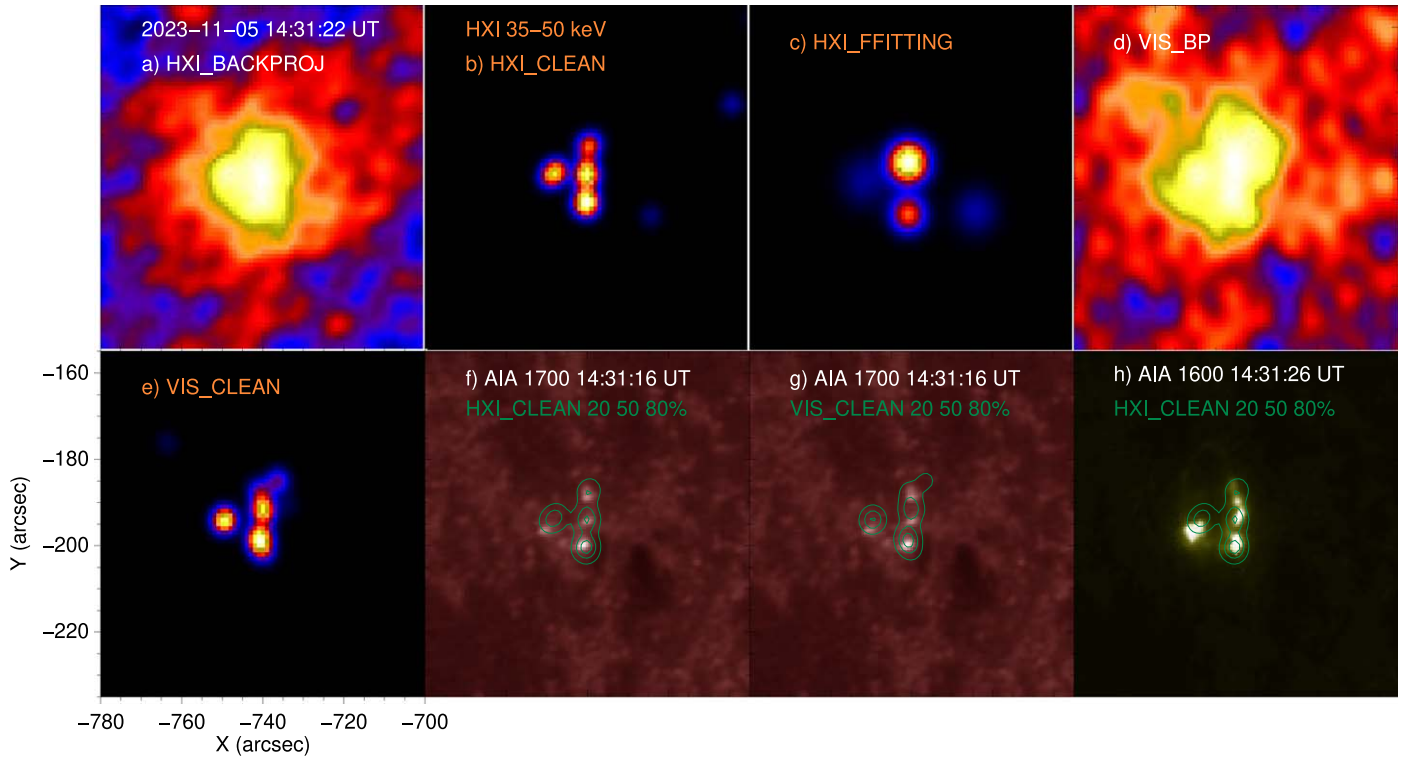

Figure 12. The reconstructed HXI images for the M1.7 flare observed on 2023 November 5. Panels (a)–(e) show the HXI images of different algorithms for 35–50 keV and the time 2023 November 5 14:31:22 UT reconstructed from detectors G2–G10. These images have a time interval of 22 s and cover an FOV of 129 × 129 pixels, with a pixel size of 1″. Panels (f) and (g) display AIA 1700 Å images with contours of HXI_CLEAN and HXI_VIS_CLEAN sources, respectively. Panel (h) shows AIA 1600 Å with contours of the HXI_CLEAN image.

Table 6
The Imaging Dynamic Range Test of Two Point Sources for HXI, Including the Flux Ratio R_{12} of the Two Sources in the Models and Reconstructed Images Corresponding to Figure 15

R	50:1	45:1	40:1	30:1	20:1	15:1	10:1	5:1	2:1
total	113.222	92.925	72.871	45.334	34.772	27.273	13.710	5.741	2.081
peak	54.320	48.857	43.322	32.179	21.470	15.948	10.4485	5.117	2.016

for imaging and $\mathrm{CBWF_{HXI}}$, $\sigma \sim \frac{R_{\mathrm{HXI}}}{\mathrm{CBWF_{HXI}}}$, where the definition of $\mathrm{CBWF_{HXI}}$ is slightly different from that for RHESSI. Using the same method presented in Section 4.4, we obtained the test results for $\mathrm{CBWF_{HXI}}$ (Figure 16). Excluding the smallest source, we get the average value of 2.49 ± 0.231, or roughly 2.5. This value will be used as the default setting for the CBWF in the next version (V1.50 beta) of the HXI analysis software.

6. Discussion and Conclusions

6.1. Forward Fit Methods

Parametric imaging schemes FF and VF differ from other algorithms in two aspects. They require prior assumptions on the shapes and numbers of sources, and they perform parameter fitting to obtain best-fit parameters and images. Therefore, they are thought to be very useful in getting source parameters. However, we encountered some problems in our tests. FF cannot correctly restore the size and orientation of the loop source. In Table 4, the flux ratios of the two sources are not as good as those obtained in other methods.

In the VF image in Figure 2, the narrow loop source tends to split into multiple sources but it effectively reproduced the characteristic of narrow sources, similar to the findings in Dennis & Tolbert (2019). The two sources are occasionally identified as one large source, similar to the case in Figure 4 in Volpara et al. (2022). Adding more restrictions, such as the location and flux of the source, could result in better images. The flux ratio of VF sources in Table 4 is similar to the model due to the utilization of location constraints. However, when the two sources have the

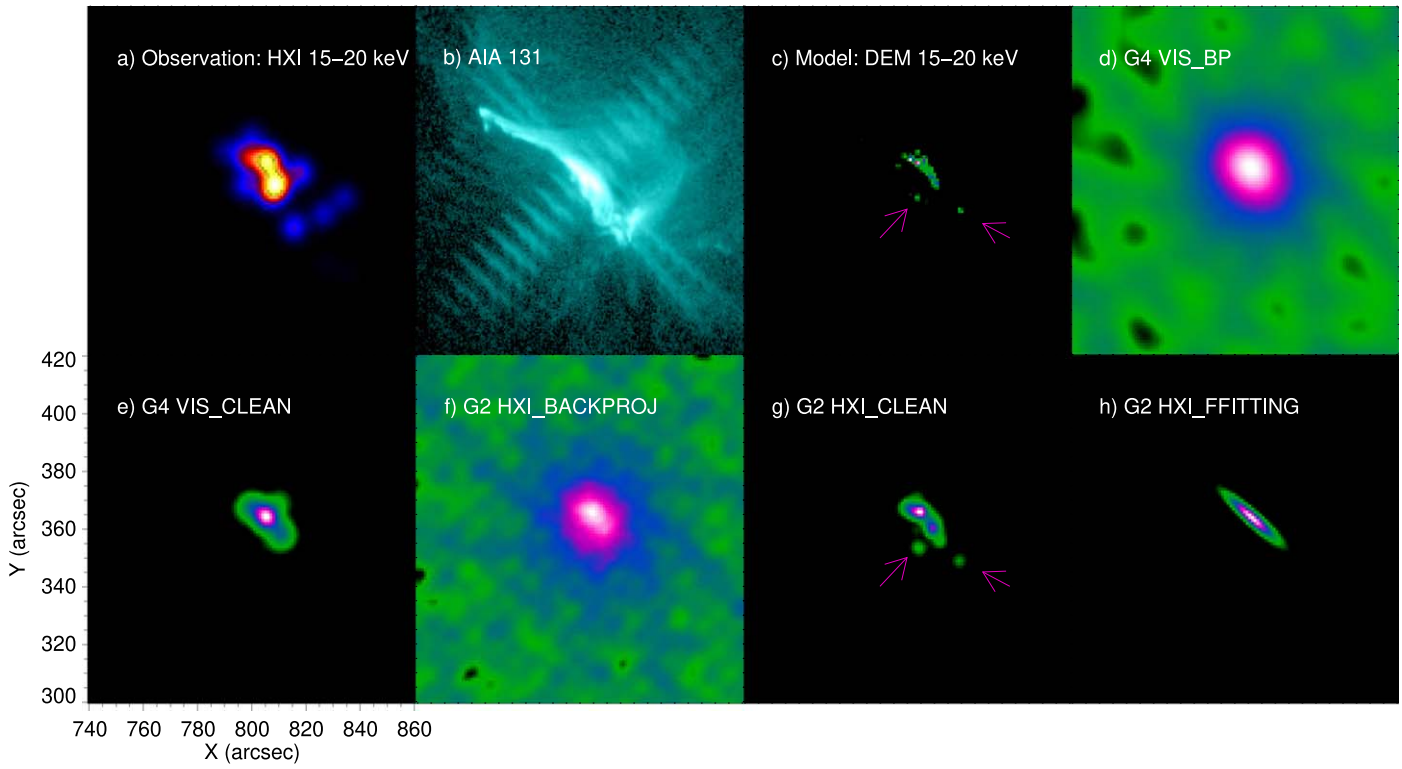

Figure 13. DEM-X test for HXI imaging algorithms. Panel (a) shows the reconstructed HXI_CLEAN image in 15–20 keV with detectors G3–G10 for the time at 2023 March 5 21:32:40 UT. Panel (b) shows the AIA 131 Å image taken at 21:32:58 UT. Panel (c) is the calculated DEM-X 15–20 keV image and also the input model for the simulation test. The images of different algorithms are shown in Panels (d)–(h). The magenta arrows point to the two weak sources.

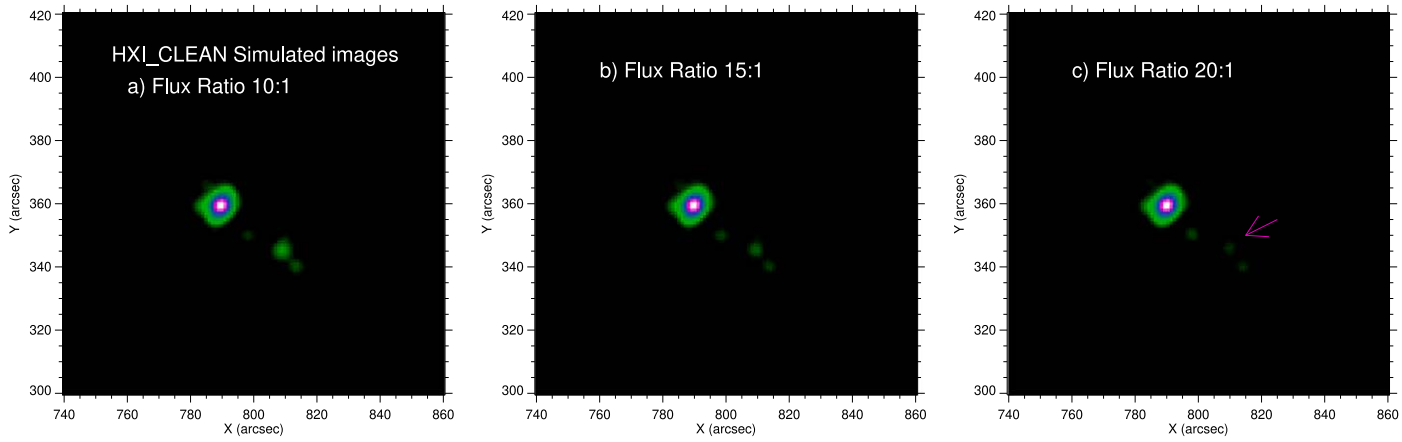

Figure 14. Reconstructed HXI_CLEAN images for the simulation cases of two footpoint sources with different flux ratios. The flux of the left source remains constant, while the flux of the weaker source on the right varies. The position of the weak source is indicated by the magenta arrow. The simulated input flux ratios are 10:1, 15:1, and 20:1. Correspondingly, the imaging results yielded the total flux (within 5% contour) ratio of 27:1, 56:1, and 207:1, and the peak flux ratio of 15:1, 26:1, and 41:1, respectively.

same flux but different areas, the sizes of the two sources in the imaging results may not be retrieved correctly.

The problems we encountered highlight the fact that an increase in the number of sources and complexity of source shapes can lead to greater uncertainties in imaging. FF (the current version) is limited in terms of setting the shape and number of sources, while in VF one can set additional restrictions for each source to optimize images. In practical imaging, constraints can come from images of other algorithms. Therefore, VF seems to be a better choice than FF for imaging with RHESSI data.

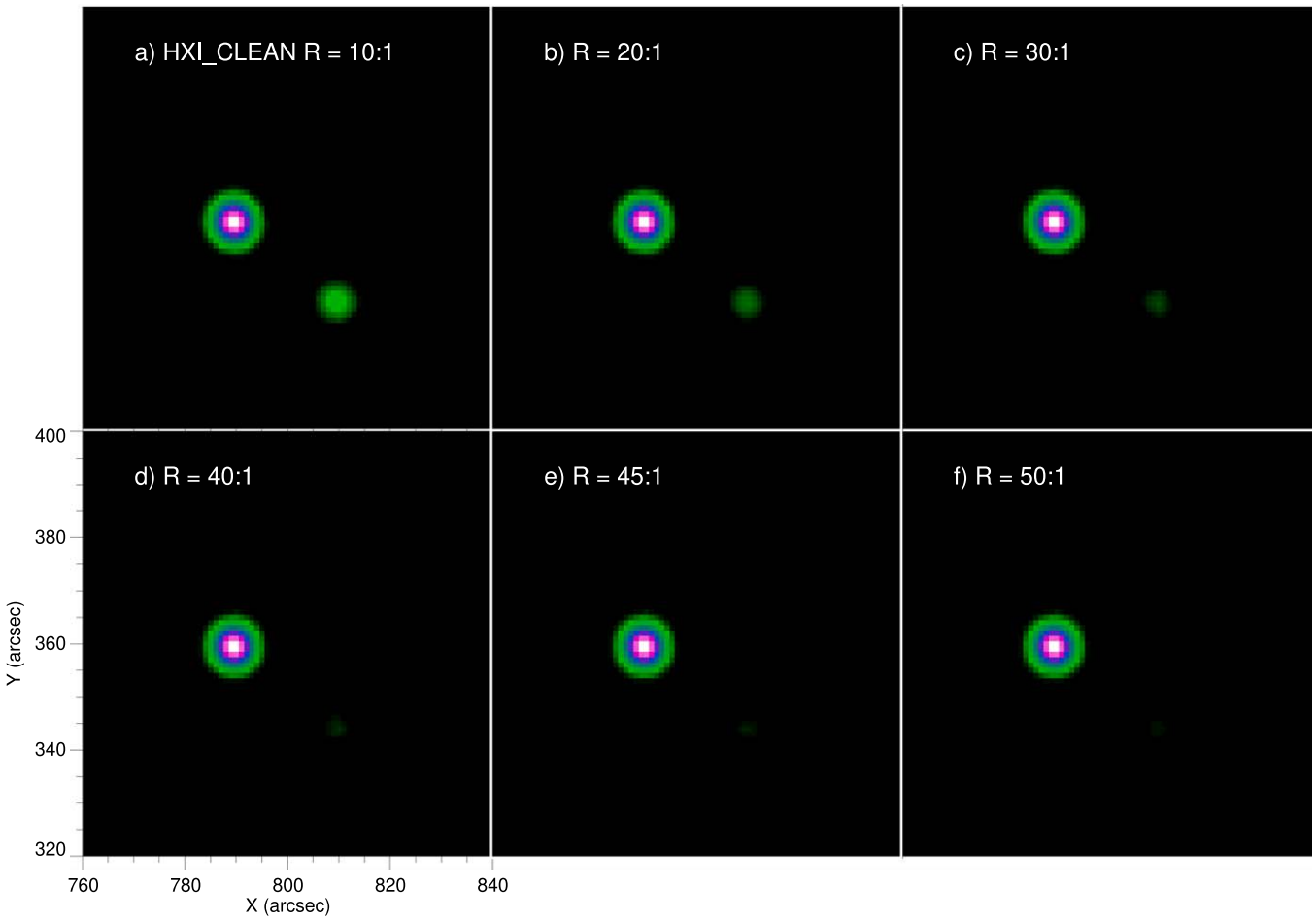

Figure 15. Reconstructed HXI_CLEAN images for the simulation case of two point sources with different flux ratios. The flux of the left source remains constant, while the flux of the weaker source on the right varies. The simulated input flux ratios are from 10:1 to 50:1.

6.2. Conclusions

A good, robust algorithm needs to reconstruct images effectively from limited data and determine accurately the source's flux, position, shape, and ideally the detailed structures of the source without producing non-physical results, such as super-resolution effects and sidelobes. However, due to the constraints of indirect X-ray imaging, including the limited number of subcollimators/visibilities and limited imaging dynamic range, it is a challenge for all the algorithms. Quantitative comparisons between reconstructed images from different algorithms and the input image (ground truth) are therefore important for understanding the advantages and limitations of each algorithm.

In this work, we used three evaluation indices, i.e., χ^2, Cstat, and the new X-ray imaging quality evaluation parameter QuIX, to analyze all RHESSI algorithms in four different imaging simulation cases, including realistic source, double sources, imaging dynamic range, and CLEAN beam size. We also tested the ASO-S/HXI algorithms with observational data and simulated sources for a better understanding of HXI imaging capability. In addition, we determined the appropriate default setting of CBWF for both RHESSI and HXI based on the simulation results of a series of single sources with different sizes, which significantly improved the imaging result compared to that from the original default CBWF = 1. However, it should be pointed out that the best value of CBWF also depends on the source structures, source sizes, and detector selection. Therefore, users are encouraged to adjust CBWF whenever needed.

In essence, most of the algorithms perform well. The EM algorithm stays reliable in most tests. The intuitive comparison between the images and the model, as well as the quantitative description, are all good. Besides, EM does not need extra parameters. The drawbacks are the loss of source information due to slight super-resolution effects and the time-consuming imaging process. CLEAN and PIXON can achieve similar high-quality images compared with EM. CLEAN needs a

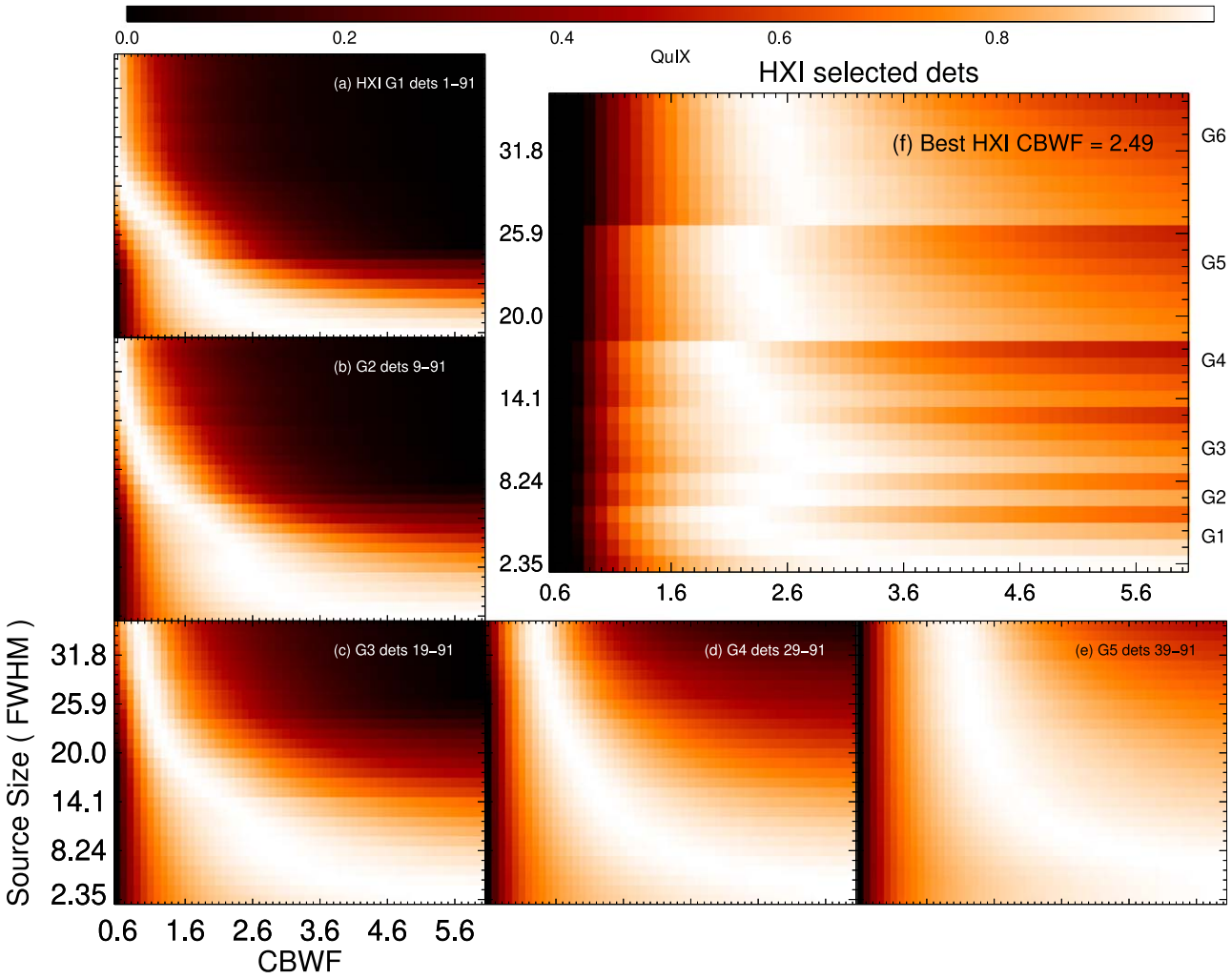

Figure 16. QuIX results of the CBWF test for HXI. Panels (a)–(e) show the results with G1-5 as the finest grids (starting subcollimator group for imaging). Panel (f) presents the result of the detector combinations suitable for each of the source sizes. The best CBWF is found around 2.2–2.8. The detector label on the right side of (f) shows the starting detector (the finest grid) selected for the imaging of sources with different FWHM.

proper setting of some parameters to get the best results, which can be complicated or even tricky as in some cases the best parameter settings are still unknown (for example, the method to add back the residual map). PIXON simultaneously possesses accurate image photometry (e.g., Aschwanden et al. 2004; Dennis & Pernak 2009) and excellent source morphology details, but sidelobes occasionally occur. Another deficiency is the time-consuming imaging process.

MEM_NJIT sources often break up, which has been pointed out by a number of studies. Its super-resolution effect can produce good images for small sources, whereas it may bring non-physical results in large sources. Massa et al. (2020) confirmed the super-resolution properties of the Maximum Entropy algorithm using STIX simulation data. As an improved version of MEM_NJIT, MEM_GE sources rarely break up. In our RHESSI tests, MEM_GE effectively balanced the super-resolution effects introduced by the algorithm with the actual source size, but sidelobes are complicated in some cases.

VIS_WV and VIS_CS perform equally, slightly worse than EM. The shape of VIS_WV central source is good, and noise or sidelobes often appear at the edges of the imaging FOV (Figures 5 and 6). VIS_CS has a cleaner background, but the shape of the source occasionally deviates. For example, the loop is recognized as footpoints in Figure 2. The robust photometry results are consistent with those reported by Felix et al. (2017).

The UV_Smooth results are not as good as other algorithms except FF and VF. In almost every test, we observe sidelobes around the sources, and the source size is also larger than the input size. However, the newly developed version of UV_Smooth by the STIX team has been optimized in this aspect (Perracchione et al. 2021).

Unlike other algorithms, the FF and VF need assumptions regarding the number and shape of sources in advance. VF performs better than FF. It allows for the setting of more parameters to constrain the imaging results. Before using FF and VF, it is better to first check on the images of other algorithms, as they provide more source information for setting the initial parameters.

Overall, the difference between our study and Dennis & Tolbert (2019) lies in the fact that we tested sources of varying sizes and shapes, including the realistic sources estimated from AIA DEM maps. A narrower source does not necessarily imply better imaging quality. Non-physical super-resolution effects can lead to information loss for larger sources, such as those observed with EM and MEM_NJIT. The resolution of the detectors remains a more crucial parameter. According to the test results, EM and PIXON provide overall the best imaging quality. CLEAN, VIS_CS, VIS_WV and MEM_GE also perform well in the reconstruction of source structures. MEM_NJIT can produce good results when the SNR is high. VF, CLEAN, PIXON and MEM_NJIT provide relatively good estimates of the total flux of individual sources and therefore can be used for imaging spectroscopy.

Based on our tests on CBWF, we recommend a default setting of CBWF = 2.2 for RHESSI to replace the original default CBWF of 1. For HXI, we suggest a default setting of CBWF = 2.5 (a slightly different definition of CBWF). Note that these best values are obtained under certain test conditions, i.e., from images made with a selected set of detectors (subcollimators) that provides comparable detector resolution to the size of a single Gaussian source. Readers may still need to explore the best combinations of CBWF and detector selection (see Figures 11 and 16) for imaging different sizes/shapes/numbers of sources with observational data.

It should also be pointed out that bad imaging quality does not necessarily mean that the algorithms are meaningless or useless. Comparing and contrasting the results obtained from different algorithms can help in verifying their accuracy and reliability. Through testing various algorithms, we expound their characteristics, advantages and disadvantages, application conditions, and some parameters that affect the images. These results can provide valuable guidance to users and support the ongoing development of HXI algorithms.

Acknowledgments

The work is supported by the National Key R&D Program of China 2022YFF0503002, the National Natural Science Foundation of China (NSFC, Grant Nos. 12333010 and 12233012), and the Strategic Priority Research Program of the Chinese Academy of Sciences (grant No. XDB0560000). Z.L. is supported by the Prominent Postdoctoral Project of Jiangsu Province (2023ZB304). ASO-S mission is supported by the Strategic Priority Research Program on Space Science, the Chinese Academy of Sciences, grant No. XDA15320000. RHESSI is a NASA Small Explorer Mission. SDO/AIA data are obtained from the JSOC Data Archive.

ORCID iDs

Wenhui Yu https://orcid.org/0009-0004-2847-9540
Yang Su https://orcid.org/0000-0002-4241-9921
Zhentong Li https://orcid.org/0000-0002-4230-2520
Wei Chen https://orcid.org/0000-0001-5279-3266
Weiqun Gan https://orcid.org/0000-0001-9979-4178

References

Aschwanden, M. J., Metcalf, T. R., Krucker, S., et al. 2004, SoPh, 219, 149
Aschwanden, M. J., Schmahl, E.RHESSI Team, et al. 2002, SoPh, 210, 193
Benvenuto, F., Schwartz, R., Piana, M., & Massone, A. M. 2013, A&A, 555, A61
Brown, J. C., McArthur, G. K., Barrett, R. K., McIntosh, S. W., & Emslie, A. G. 1998, SoPh, 179, 379
Cash, W. 1979, ApJ, 228, 939
Cheung, M. C. M., Boerner, P., Schrijver, C. J., et al. 2015, ApJ, 807, 143
Dennis, B. R., & Pernak, R. L. 2009, ApJ, 698, 2131
Dennis, B. R., & Tolbert, A. K. 2019, ApJ, 887, 131
Duval-Poo, M. A., Piana, M., & Massone, A. M. 2018, A&A, 615, A59
Felix, S., Bolzern, R., & Battaglia, M. 2017, ApJ, 849, 10
Gan, W., Zhu, C., Deng, Y., et al. 2023, SoPh, 298, 68
Gan, W.-Q., Zhu, C., Deng, Y.-Y., et al. 2019, RAA, 19, 156
Hannah, I. G., Christe, S., Krucker, S., et al. 2008, ApJ, 677, 704
Harrison, F. A., Craig, W. W., Christensen, F. E., et al. 2013, ApJ, 770, 103
Högbom, J. A. 1974, A&AS, 15, 417
Holman, G. D., Aschwanden, M. J., Aurass, H., et al. 2011, SSRv, 159, 107
Hurford, G. J., Schmahl, E. J., & Schwartz, R. A. 2005, AGU Spring Meeting Abstracts, 2005, SP21A
Hurford, G. J., Schmahl, E. J., Schwartz, R. A., et al. 2002, SoPh, 210, 61
Hwang, C.-L., & Yoon, K. 1981, Methods for Multiple Attribute Decision Making, Multiple Attribute Decision Making: Methods and Applications A State-of-the-art Survey (Berlin: Springer), 58
Kontar, E. P., Hannah, I. G., Jeffrey, N. L. S., & Battaglia, M. 2010, ApJ, 717, 250
Kosugi, T., Makishima, K., Murakami, T., et al. 1991, SoPh, 136, 17
Krucker, S., Christe, S., Glesener, L., et al. 2014, ApJL, 793, L32
Krucker, S., Hurford, G. J., Grimm, O., et al. 2020, A&A, 642, A15
Lemen, J. R., Title, A. M., Akin, D. J., et al. 2012, SoPh, 275, 17
Li, Z., Su, Y., Veronig, A. M., et al. 2022, ApJ, 930, 147
Li, Z., Yu, W., Su, Y., Chen, W., & Gan, W. 2024, RAA, Submitted
Lin, R. P., Dennis, B. R., Hurford, G. J., et al. 2002, SoPh, 210, 3
Massa, P., Piana, M., Massone, A. M., & Benvenuto, F. 2019, A&A, 624, A130
Massa, P., Schwartz, R., Tolbert, A. K., et al. 2020, ApJ, 894, 46
Massone, A. M., Emslie, A. G., Hurford, G. J., et al. 2009, ApJ, 703, 2004
Mertz, L. N., Nakano, G. H., & Kilner, J. R. 1986, JOSAA, 3, 2167
Metcalf, T. R., Hudson, H. S., Kosugi, T., Puetter, R. C., & Pina, R. K. 1996, ApJ, 466, 585
Perracchione, E., Massa, P., Massone, A. M., & Piana, M. 2021, ApJ, 919, 133
Piana, M., Emslie, A., Massone, A., & Dennis, B. 2022, Hard X-Ray Imaging of Solar Flares (Cham: Springer)
Schmahl, E. J., Pernak, R. L., Hurford, G. J., Lee, J., & Bong, S. 2007, SoPh, 240, 241
Schwartz, R. A., Csillaghy, A., Tolbert, A. K., et al. 2002, SoPh, 210, 165
Su, Y., Liu, W., Li, Y.-P., et al. 2019, RAA, 19, 163
Su, Y., Veronig, A. M., Hannah, I. G., et al. 2018, ApJL, 856, L17
Su, Y., Zhang, Z., Chen, W., et al. 2024, SoPh, 299, 153
Volpara, A., Massa, P., Perracchione, E., et al. 2022, A&A, 668, A145
Warmuth, A., & Mann, G. 2013, A&A, 552, A86
Xia, Y., Su, Y., Liu, H., et al. 2024, SoPh, 299, 158
Zhang, Z., Chen, D.-Y., Wu, J., et al. 2019, RAA, 19, 160